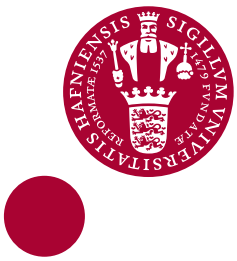

Structural Basis of Membrane Protein Chaperoning through the Mitochondrial Intermembrane Space

Weinhaupl, Katharina; Lindau, Caroline; Hessel, Audrey; Wang, Yong; Schültze, Conny; Jores, Tobias; Melchionda, Laura; Schönfisch, Birgit; Kalbacher, Hubert; Bersch, Beate; Rapaport, Doron; Brennich, Martha; Lindorff-Larsen, Kresten; Wiedemann, Nils; Schanda, Paul

Published in:
Cell

DOI:
10.1016/j.cell.2018.10.039

Publication date:
2018

Document version
Publisher's PDF, also known as Version of record

Article

Cell

Structural Basis of Membrane Protein Chaperoning through the Mitochondrial Intermembrane Space

Graphical Abstract

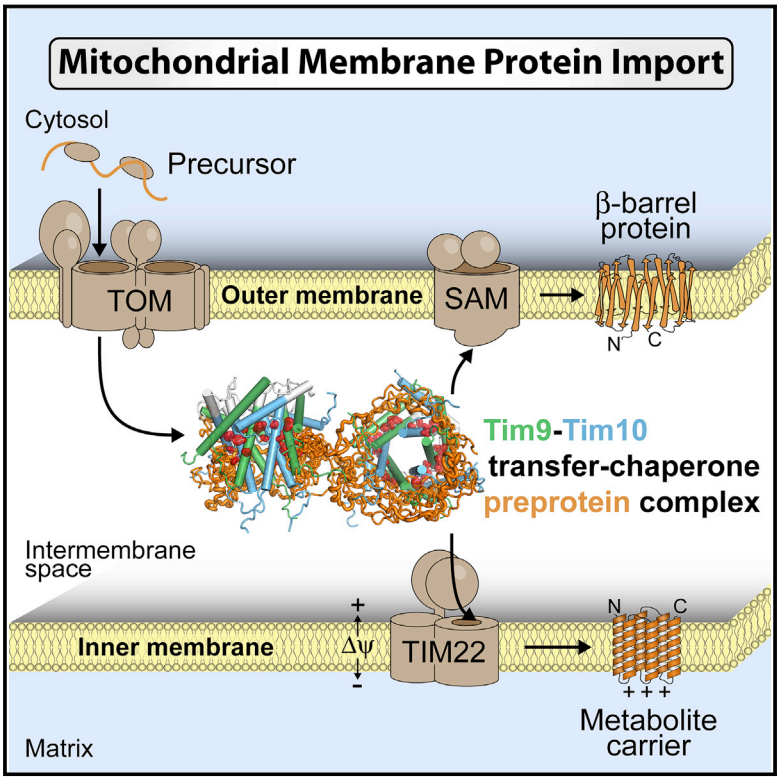

Highlights

- Structural and *in vivo* data reveal basis of membrane protein "transfer-chaperone"
- Multiple clamp-like binding sites hold the precursors in an elongated conformation
- Tight complex results from dynamic contacts with numerous precursor conformations
- Transfer of precursors in partial α-helical or β-hairpin conformation to insertases

Authors

Katharina Weinhäupl, Caroline Lindau, Audrey Hessel, ..., Kresten Lindorff-Larsen, Nils Wiedemann, Paul Schanda

Correspondence

nils.wiedemann@biochemie.uni-freiburg.de (N.W.), paul.schanda@ibs.fr (P.S.)

In Brief

Structural and mechanistic studies of TIM chaperones reveal how they hold client proteins in a nascent chain-like extended conformation to facilitate insertion into the mitochondrial inner or outer membrane.

Weinhäupl et al., 2018, Cell *175*, 1365–1379
November 15, 2018
https://doi.org/10.1016/j.cell.2018.10.039

CellPress

Article

Cell

Structural Basis of Membrane Protein Chaperoning through the Mitochondrial Intermembrane Space

Katharina Weinhäupl,[1,8] Caroline Lindau,[2,3,8] Audrey Hessel,[1] Yong Wang,[4] Conny Schütze,[2] Tobias Jores,[5] Laura Melchionda,[2] Birgit Schönfisch,[2] Hubert Kalbacher,[5] Beate Bersch,[1] Doron Rapaport,[5] Martha Brennich,[6] Kresten Lindorff-Larsen,[4] Nils Wiedemann,[2,7,*] and Paul Schanda[1,9,*]

[1]Institut de Biologie Structurale (IBS), Univ. Grenoble Alpes, CEA, CNRS, 71 Avenue des Martyrs, 38000 Grenoble, France
[2]Institute of Biochemistry and Molecular Biology, ZBMZ, Faculty of Medicine, University of Freiburg, 79104 Freiburg, Germany
[3]Faculty of Biology, University of Freiburg, 79104 Freiburg, Germany
[4]Structural Biology and NMR Laboratory, the Linderstrøm-Lang Centre for Protein Science, Department of Biology, University of Copenhagen, 2200 Copenhagen, Denmark
[5]Interfaculty Institute of Biochemistry, University of Tübingen, 72076 Tübingen, Germany
[6]European Molecular Biology Laboratory, 38042 Grenoble, France
[7]BIOSS Centre for Biological Signalling Studies, University of Freiburg, 79104 Freiburg, Germany
[8]These authors contributed equally
[9]Lead Contact
*Correspondence: nils.wiedemann@biochemie.uni-freiburg.de (N.W.), paul.schanda@ibs.fr (P.S.)
https://doi.org/10.1016/j.cell.2018.10.039

SUMMARY

The exchange of metabolites between the mitochondrial matrix and the cytosol depends on β-barrel channels in the outer membrane and α-helical carrier proteins in the inner membrane. The essential translocase of the inner membrane (TIM) chaperones escort these proteins through the intermembrane space, but the structural and mechanistic details remain elusive. We have used an integrated structural biology approach to reveal the functional principle of TIM chaperones. Multiple clamp-like binding sites hold the mitochondrial membrane proteins in a translocation-competent elongated form, thus mimicking characteristics of co-translational membrane insertion. The bound preprotein undergoes conformational dynamics within the chaperone binding clefts, pointing to a multitude of dynamic local binding events. Mutations in these binding sites cause cell death or growth defects associated with impairment of carrier and β-barrel protein biogenesis. Our work reveals how a single mitochondrial "transfer-chaperone" system is able to guide α-helical and β-barrel membrane proteins in a "nascent chain-like" conformation through a ribosome-free compartment.

INTRODUCTION

The vast majority of mitochondrial membrane proteins are synthesized on cytosolic ribosomes and subsequently imported into the organelle by the translocase of the outer membrane (TOM) (Dolezal et al., 2006; Neupert and Herrmann, 2007; Wiedemann and Pfanner, 2017). Mitochondrial β-barrel and metabolite carrier precursor proteins with multiple transmembrane segments are sorted through the intermembrane space (IMS) to get engaged with their dedicated membrane integration machineries. β-barrel membrane proteins are inserted by the sorting and assembly machinery at the outer membrane (SAM/TOB) (Paschen et al., 2003; Wiedemann et al., 2003) and metabolite carrier proteins by the carrier translocase of the inner membrane (TIM22) in a manner that is dependent on the potential ($\Delta\psi$) across the inner membrane (Kerscher et al., 1997; Rehling et al., 2003; Sirrenberg et al., 1996). The mitochondrial IMS contains a single chaperone system comprising the small Tim proteins, Tim8, Tim9, Tim10, Tim12, and Tim13 (Koehler et al., 1998; Sirrenberg et al., 1998; Vial et al., 2002). The TIM chaperone system is crucial to mediate the transfer of some of the most abundant mitochondrial membrane protein precursors from the TOM complex to either SAM or the TIM22 complexes (Morgenstern et al., 2017). The mitochondrial IMS assembly machinery MIA covalently links the twin CX_3C cysteine motif of the TIM chaperone proteins by introducing disulfide bonds, such that both N- and C-terminal α-helical segments form a cleft (Chacinska et al., 2004; Mesecke et al., 2005).

High-resolution structures show that the soluble TIM chaperone complexes assemble as alternating circular hexamers formed by three subunits of each Tim9 and Tim10, or Tim8 and Tim13 for the TIM9·10 and TIM8·13 chaperones, respectively (Beverly et al., 2008; Webb et al., 2006). The TIM22 complex contains an additional translocase-bound form composed of the three essential TIM chaperone proteins Tim9, Tim10, and Tim12, which constitute a specific complex for the insertion of inner membrane precursors (Koehler et al., 1998; Lionaki et al., 2008; Sirrenberg et al., 1998). In contrast, the soluble TIM8·13 complex is considered to be redundant to the TIM9·10 complex in the intermembrane space (Habib et al., 2005; Hoppins and Nargang, 2004; Wiedemann et al., 2004). Nonetheless, mutations affecting the human Tim8 homolog DDP1 are associated with the mitochondrial neuronopathy called Mohr-Tranebjærg or deafness dystonia syndrome (Koehler et al., 1999).

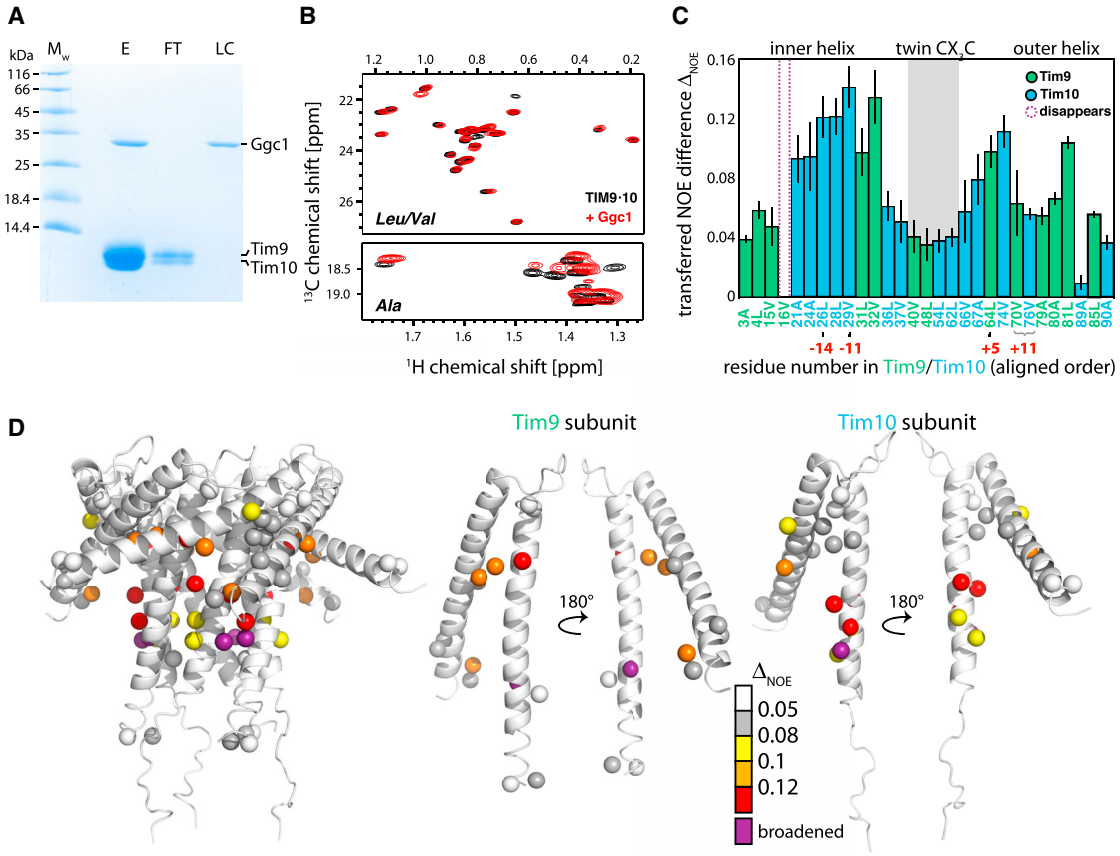

Figure 1. Inner Membrane Precursor Proteins Bind in a Hydrophobic Cleft of TIM9·10

(A) *In vitro* formation of the TIM9·10/Ggc1 complex by a Ni-NTA based pull-down approach, monitored by SDS-PAGE analysis and Coomassie staining. FT, flow-through; E, TIM9·10/Ggc1 fraction eluted from the column with imidazole; LC, loading control (subsequent imidazole-elution with guanidine hydrochloride of Ggc1 not bound by TIM9·10).

(B) Methyl ^{1}H-^{13}C HMQC NMR spectra of apo and Ggc1-bound ALV-labeled TIM9·10.

(C) Transferred NOE effects from protonated Ggc1 to deuterated, ALV-labeled TIM9·10 as a function of the TIM9·10 methyl residue number. The resonance of V16 (purple, dashed) is broadened beyond detection upon Ggc1 binding. Error bars were determined from the spectral noise level and error propagation (see STAR Methods).

(D) Structural view of the transferred NOE data from (C).

See also Figure S1.

It is currently unknown how the TIM chaperones bind various membrane protein precursors and manage their transfer to their corresponding target membrane, also leaving the molecular basis of this chaperone-related disease unclear. Four major models for TIM chaperone function have been proposed (Beverly et al., 2008; Martín-Benito et al., 2007; Vergnolle et al., 2005; Webb et al., 2006): (1) binding of the substrate in the central cavity formed by the tentacle-like inner N termini, similar to the structurally unrelated chaperone prefoldin in the cytosol and Skp in the bacterial periplasm; (2) intercalation of a metabolite carrier helix-loop-helix motif in opposing orientation to a Tim chaperone monomer, referred to as ''bisecting dimerization''; (3) incorporation of hydrophobic substrate helices into the TIM chaperone ring structure by competitive Tim subunit displacement; and (4) natively folded substrate wedged within the N-terminal tentacles. However, complexes of TIM chaperones with the aggregation-prone membrane proteins in transit have remained elusive, due to the challenge of preparing and characterizing such complexes *in vitro* and the difficulty of obtaining structural insights into chaperone/client protein complexes. The structure, dynamics, and interactions of this complex remain unresolved.

RESULTS

Nuclear Magnetic Resonance Reveals the Binding of Precursor Proteins to the Mitochondrial TIM Chaperones

To gain structural insight into the chaperone mechanism, we developed *in vitro* protocols to reconstitute recombinantly expressed carriers with the TIM9·10 chaperone. Samples for structural studies were prepared by attaching unfolded carriers to a metal-affinity resin, addition of TIM9·10 and elution of the chaperone/precursor protein complex (Figure 1A). In an orthogonal approach, we produced the GDP/GTP carrier

Ggc1/TIM9·10 complex by *in vitro* translation (Figure S1A). These findings establish that recombinant TIM9·10 is able to bind the precursor proteins in an unfolded form as well as polypeptide exiting the ribosome. Nuclear magnetic resonance (NMR) spectra of TIM9·10 carrying either Ggc1 or Aac3 (ADP/ATP carrier, or adenine nucleotide translocator) feature cross-peak positions that are similar to those of apo TIM9·10 (Figures 1B and S1B–S1D). The similarity of apo and holo complex spectra establishes that the hexameric chaperone remains structurally intact upon membrane protein binding, excluding models in which either monomeric Tim chains bind to precursor proteins or in which α helices of the carrier precursor protein intercalate in between the subunits of the oligomeric chaperone (Webb et al., 2006). Interestingly, only a single set of cross-peaks is observed, indicating that each of the symmetry-related Tim subunits in the hexameric complex adopts the same conformation and precursor interaction on the fast-exchange NMR timescale (i.e., up to the ms [ms] timescale). Local asymmetry is averaged out on the sub-ms timescale. The resonance peak intensities in samples of TIM9·10 bound to carrier proteins are reduced compared to apo TIM9·10, in particular for backbone NH sites (Figures S1E–S1G). As outlined below, the strongly reduced NMR peak intensity can be ascribed to the larger size and conformational dynamics of the TIM/precursor protein complexes.

For further structural investigations, we exploited the intrinsically higher detection sensitivity of methyl groups and used deuterated samples with $^{13}CH_3$-labeling at Ala, Leu, and Val (ALV) side chains. We identified the binding sites of the precursor protein on the TIM hexamer through NMR saturation-transfer methods, which probe the spatial proximity of hydrogen atoms on Ggc1 to ALV methyl groups on TIM9·10 (Figures 1C and 1D). Residues with the strongest transferred-nuclear Overhauser effects (NOE) are located in the cleft formed between the N- and C-terminal helices. To obtain independent insight into the precursor protein binding, we used paramagnetic NMR experiments in which we attached a paramagnetic spin label to Ggc1, either in a transmembrane helix (residue 222) or at the N terminus (residue 8), and monitored how the Ggc1-bound spin label enhances the spin relaxation of ALV sites on TIM9·10. In agreement with the saturation-transfer data, the largest PRE-effects are observed for residues located in the hydrophobic cleft (Figures S1H–S1K).

We then investigated whether precursors of outer-membrane β-barrel proteins use the same interaction cleft of TIM9·10. The methods, which were successfully used for generating complexes with inner-membrane precursor proteins, failed to yield stable complexes with full-length β-barrel precursors, suggesting that these complexes are less stable. However, we succeeded in analyzing the binding of a peptide fragment of the voltage-dependent anion channel (VDAC) comprising the two C-terminal β strands, $VDAC_{257–279}$, to TIM9·10. Both cross-linking (Figure 2A) and NMR titration experiments (Figures 2B and 2C) demonstrated that only the cyclic $VDAC_{257–279}$ peptide that adopts a β-hairpin conformation (Jores et al., 2016) interacts with the chaperone while the linear variant does not (Figures 2 and S2). This observation highlights the importance of the β-hairpin conformation for interaction. The binding site, revealed by backbone and methyl chemical-shift perturbations, comprises the same clamp-like binding cleft that interacts with inner-membrane protein precursors (Figure 2D).

Single Point Mutations in the Conserved Binding Cleft of the TIM Chaperones Impair Cell Growth and Cause Lethality

To investigate the relevance of the identified binding cleft for TIM function, we performed a sequence alignment of mitochondrial TIM chaperone proteins from yeast to human. We found that residues in this binding cleft form a conserved core motif with hydrophobic residues located at positions −14, −11, −8, and −7 before and at +5, +11, and +15 after the twin CX_3C motif (Figures 3A and S3A). The conserved hydrophobic positions point into the cleft between the N-terminal inner helix and the C-terminal outer helix (Figure 3B), which were identified by our structural NMR data as precursor binding sites. To evaluate the importance of the conserved motif *in vivo*, we performed site directed mutagenesis of the essential yeast *TIM9* and *TIM10* genes (Truscott et al., 2002). For all conserved positions in yeast Tim9 and Tim10, except for the positions −4 and +4 that form the cleft constriction (Figure S3B), the hydrophobic residues were replaced by hydrophilic amino acids. Growth of the resulting yeast *tim9* and *tim10* mutant strains was analyzed on fermentable glucose (YPD) and non-fermentable glycerol (YPG) medium (Figures 3C and S3C). The *TIM9* mutations M21S, V70K, and F74K are lethal and the mutations F24K, L27K, and Y28Q caused significant growth defects. The *TIM10* mutations L26K, V29K, M32K, F33Q, V76K, and M80K caused similar defects on both carbon sources, in agreement with the essential role of the TIM chaperones. To analyze the *in vivo* defects of these single point mutations, mitochondria were isolated by differential centrifugation from cells grown at non-permissive condition at 37°C (Figures 3C and S3C). The steady-state levels, as monitored by western blotting, of inner membrane metabolite carriers like Aac2, Dic1 (dicarboxylate carrier), and Yhm2 (citrate and oxoglutarate carrier), as well as those of the carrier-like proteins Tim22 and Tim23, were reduced in the single point mutants affecting the hydrophobic motif of either Tim9 or Tim10 (Figure 3D). This mutational analysis substantiates the relevance of the conserved TIM chaperone motif for the biogenesis of metabolite carrier proteins.

It was reported that the TIM8·13 complex has overlapping functions to those of the TIM9·10 complex in the transport of precursor proteins through the IMS (Habib et al., 2005; Hoppins and Nargang, 2004; Wiedemann et al., 2004). Upon deletion of the redundant TIM8·13 complex, we identified further single point mutations of *tim9* and *tim10* affecting the conserved motif, which are lethal (Figures 3E and S3D). Mutations causing the replacement of two residues opposing each other within the cleft between the N- and C-terminal helices V29KV76S(motif position: −11&+11), F33QF70S(−7&+5), or of two adjacent hydrophobic residues L26KV29K(−14&−11), V29KF33Q(−11&−7), and M32KF33Q(−8&−7) for *TIM10* and M21KF24K(−14&−11), L27SY28Q(−8&−7) for *TIM9* aggravated the growth defects of the single mutants (Figures 3C, 3F, and S3C) and are all lethal in the *tim8tim13*ΔΔ background (Figure 3E). In the absence of TIM8·13, the protein amounts of the tested Tim9 and Tim10 mutants are comparable to those in cells harboring the TIM8·13

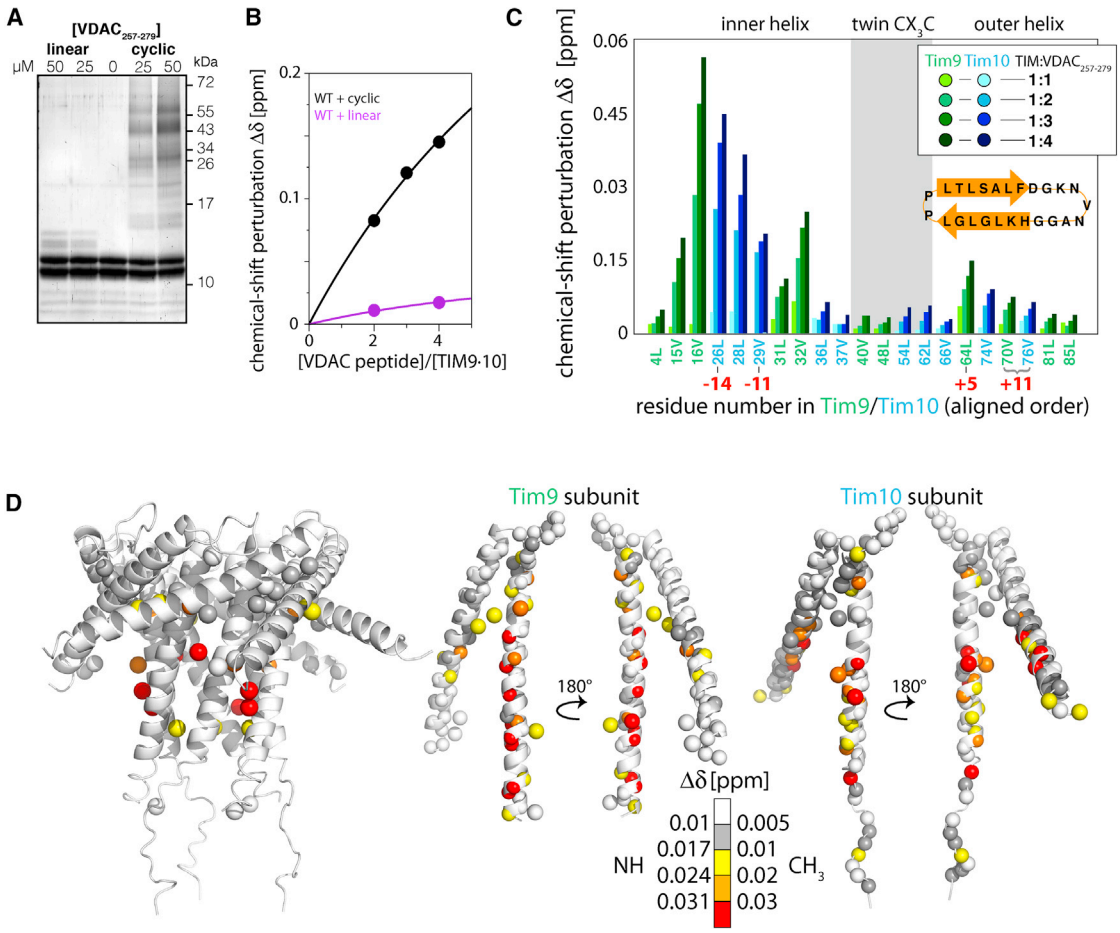

Figure 2. β-Hairpin Formation Is Important for Binding of Outer Membrane Precursor Fragments

(A) Crosslinking of Bpa-containing linear or cyclic β-hairpin peptides ($VDAC_{257–279}$) at variable concentration (indicated at the top) with the TIM9·10 complex (5 μM) detected by SDS-PAGE and silver staining.

(B) NMR chemical-shift perturbation (CSP) in wild-typeTIM9·10 upon titration with VDAC peptides. Shown is the sum of the CSPs of V16, L28, L31, V32, V70, and V74.

(C) Residue-wise CSPs in wild-type TIM9·10 upon titration with cyclic $VDAC_{257–279}$.

(D) Structural view of the cyclic-$VDAC_{257–279}$-induced CSPs.

See also Figure S2.

complex, excluding a compensatory overexpression of TIM9·10 (Figure S3E). To verify that the mutant TIM9·10 complexes are properly assembled and are not prone to clearance by the i-AAA protease (Baker et al., 2012), we expressed them in bacterial cells. We assessed their oligomerization and structure by gel filtration (Figure 3G) and NMR analysis (deposited in Mendeley data, see Key Resource Table). All tested mutants including the two Tim10 mutants V29K and M32K, which caused lethality in the absence of the TIM8·13 complex, form a stable hexameric apo chaperone complex.

Mutations Affecting the Conserved Binding Cleft of TIM Chaperones Impair the Binding and the Biogenesis of α-Helical Metabolite Carrier Proteins

To test if mutations in the conserved motif of Tim9 and Tim10 affect the transfer of hydrophobic membrane protein precursors through the IMS, mitochondria were isolated from the viable mutant strains harboring the *tim8tim13*ΔΔ background grown at permissive conditions (19°C–23°C, Figure S3D). Most mutant mitochondria contained protein amounts comparable to wild-type (WT) and contained assembled TIM22 complex (Figures S4A and S4B). $Tim9_{F24K}$ mitochondria contained not only reduced levels of inner membrane carrier proteins like Aac2 and Dic1, but also reduced levels of the essential outer membrane β-barrel protein Tom40 causing a lower accumulation of radiolabeled Oxa1 precursor at the TOM complex (Figure S4C). In contrast to the compromised levels of metabolite carrier proteins observed *in vivo* upon Tim9 and Tim10 mutations (Figure 3D), the β-barrel assembly pathway is additionally affected in the *tim8tim13*ΔΔ background ($Tim9_{F24K}$, Figure S4A). To exclude general mitochondrial defects in the other mutants, the mitochondrial membrane potential (Δψ), the import of radiolabeled precursor protein composed of the presequence of *Neurospora crassa* subunit 9 of the ATPase fused to mouse

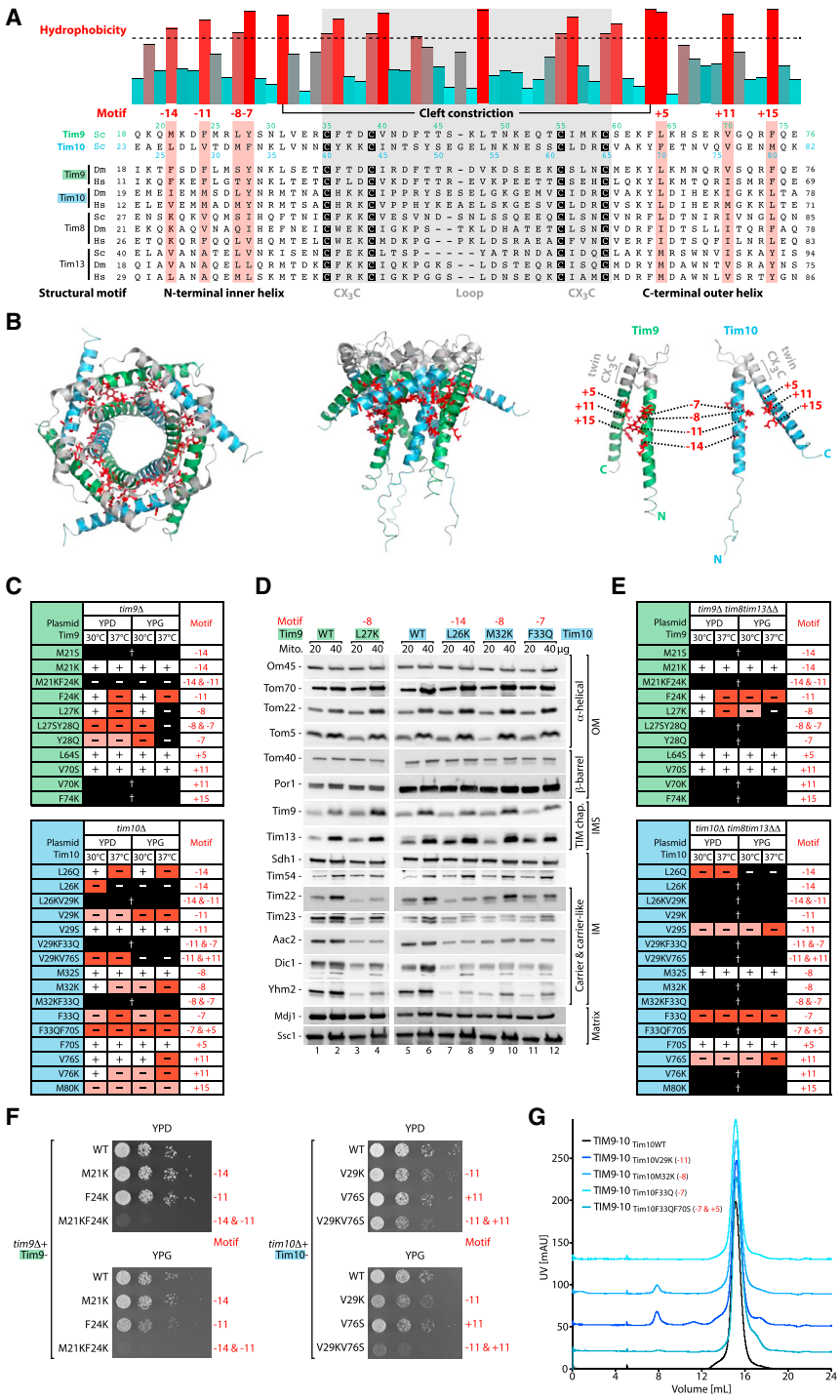

Figure 3. Point Mutations Affecting the Conserved TIM Chaperone Motif Cause Growth Defects and Lethality

(A) The bar graph shows the mean hydrophobicity of a TIM chaperone alignment highlighting a conserved motif (red). Sc, *Saccharomyces cerevisiae*; Dm, *Drosophila melanogaster*; Hs, *Homo sapiens*.

(B) Hydrophobic TIM chaperone motif plotted on the TIM9·10 structure.

(C) Growth phenotype of *tim9* and *tim10* with single point mutants affecting the conserved motif. +, no growth defect; – (red), (strong) growth defect; black, no growth; †, lethal.

(D) Protein steady-state amounts of *tim9* and *tim10* mutant mitochondria subjected to SDS-PAGE followed by immunodecoration with indicated antibodies. OM, outer mitochondrial membrane; IMS, intermembrane space; IM, inner mitochondrial membrane.

(E) Growth phenotype of *tim9* and *tim10* mutants in *tim8tim13*ΔΔ background as described in (C).

(F) Yeast growth of *tim9* and *tim10* on fermentative (YPD) or non-fermentative (YPG) medium at 30°C.

(G) Gel filtration profiles of hexameric TIM9·10 and *tim10* mutant complexes.

See also Figure S3.

dihydrofolate reductase (pSu9-DHFR) and of $F_1\beta$ (Atp2) were monitored. Both the membrane potential and the import of matrix-destined precursor proteins were comparable to wild-type for most of the analyzed mutants (Figures S3E and S4D–S4F), except for $Tim9_{V70S}$ and $Tim10_{F33Q}$, which were therefore excluded from further $\Delta\psi$-dependent analysis.

To test the ability of the TIM chaperone complex to bind to metabolite carrier substrate, import of [^{35}S]Aac2-DHFR was arrested by addition of methotrexate (Ryan et al., 1999), which causes stable folding of DHFR and thus blocks the import of the DHFR passenger domain at the TOM channel (Figures 4A and 4B). Upon binding of the wild-type TIM9·10 chaperone, the Aac2-DHFR precursor is stably arrested at the TOM complex as resolved by blue native PAGE. In contrast, the Aac2-DHFR/TOM intermediate is reduced in the mutants (Figures 4A and 4B), a finding that is ascribed to the inability of these mutants to stably hold metabolite carrier precursors. When the full import of radiolabeled metabolite carrier and carrier-like proteins was analyzed by blue native PAGE, defects in Aac2 and Tim23 inner membrane protein assembly were observed in the mutants (Figures 4C–4E). We studied the effects of these mutations on the molecular level by comparing the ability of wild-type and mutant TIM9·10 to form complexes with metabolite carrier precursor protein using the *in vitro* reconstitution approach described above (Figure 1A). While wild-type TIM forms stable complexes with Ggc1, a single amino acid mutation in each of the Tim9 or Tim10 subunits inhibits complex formation (Figure 4F). Collectively, these import

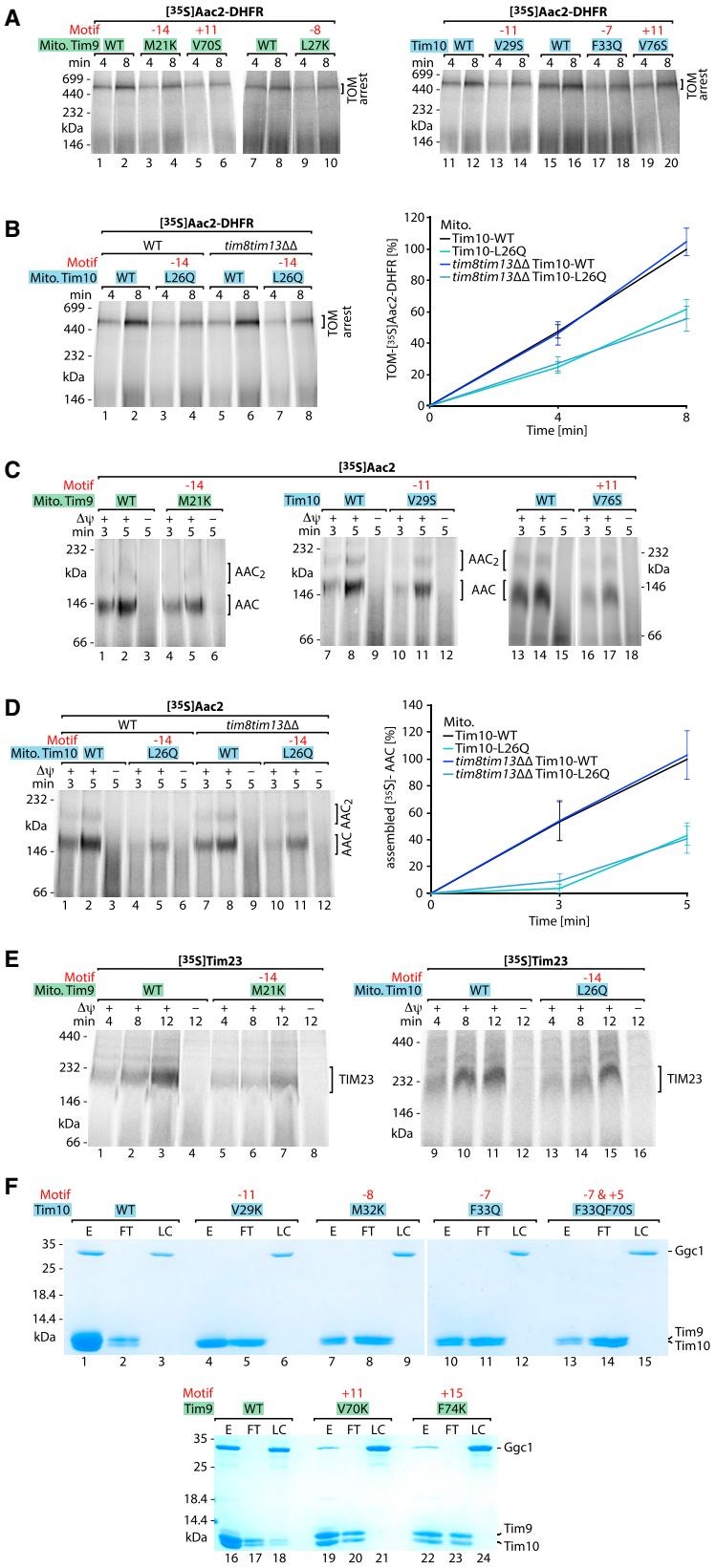

Figure 4. Metabolite Carrier Precursor Biogenesis Defects in TIM Chaperone Motif Mutants

(A and B) Methotrexate preincubated [^{35}S]Aac2-DHFR was incubated with isolated mitochondria of *tim9* and *tim10* mutants in *tim8tim13*ΔΔ (A) or indicated background (B) and analyzed by blue native PAGE and autoradiography. In (B), the Aac2-TOM intermediate was quantified by autoradiography (SEM, n = 3 experiments). TOM, translocase of the outer mitochondrial membrane.

(C) Import of [^{35}S]Aac2 analyzed without methotrexate as in (A).

(D) [^{35}S]Aac2 was imported into mitochondria from the indicated background as described in (C) and the major form of the assembled carrier (AAC) was quantified by autoradiography (SEM, n = 3 experiments). Δψ, mitochondrial membrane potential; $AAC_{(2)}$, ADP/ATP carrier$_{(oligomer)}$.

(E) Assembly of [^{35}S]Tim23 analyzed as in (C). TIM23, presequence translocase of the inner membrane.

(F) Analysis of wild-type TIM9·10, *tim9*-, and *tim10* mutant complexes as described in Figure 1A.

See also Figure S4.

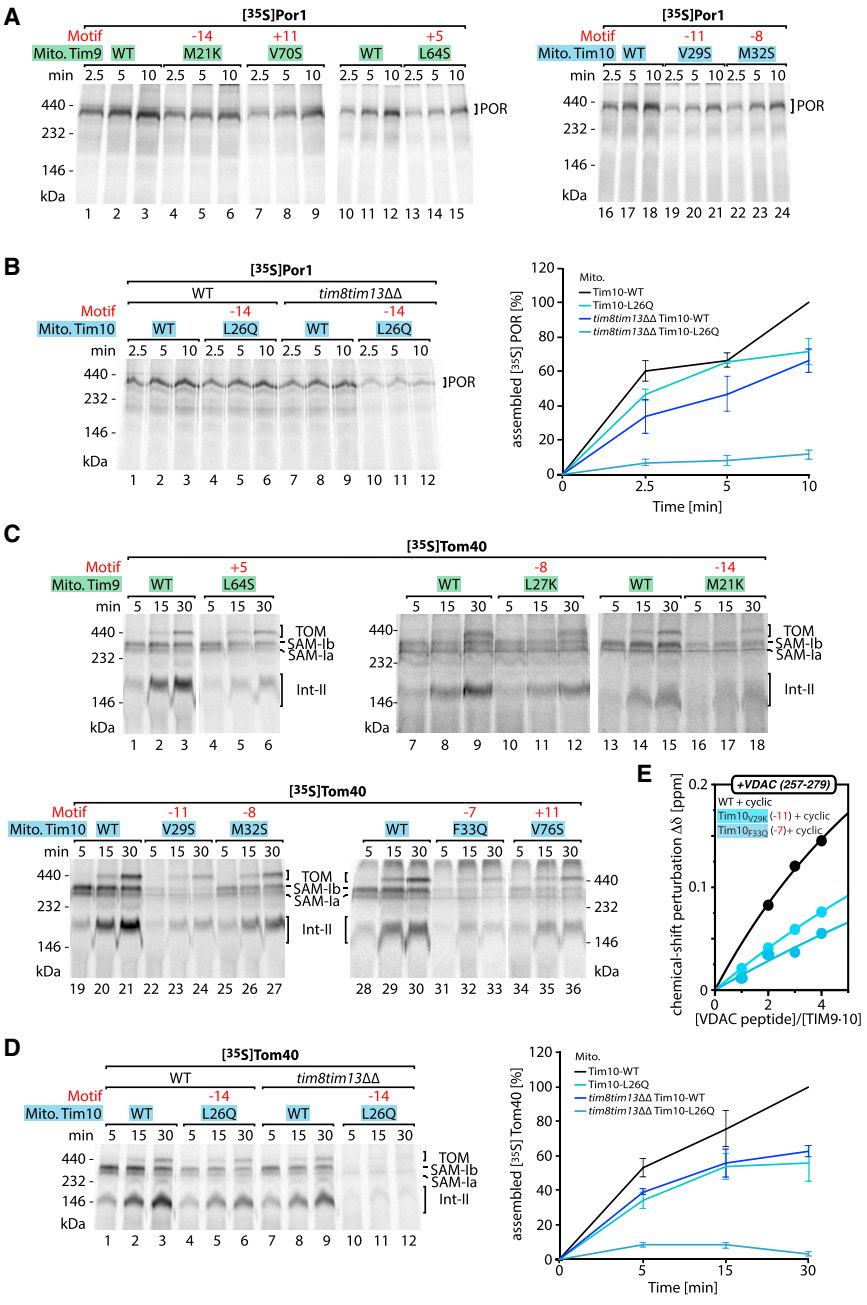

Figure 5. β-Barrel Biogenesis and Chaperone Binding Is Impaired by Mutations in the TIM Chaperone Motif

(A and B) Assembly of the porin complex, POR, was studied by incubating [^{35}S]Por1 with isolated mitochondria of *tim9* and *tim10* mutants in *tim8tim13*ΔΔ (A) or indicated background (B) followed by blue native PAGE and autoradiography analyses. In (B), the assembled POR was quantified by autoradiography (SEM, n = 3 experiments).

(C) Assembly of [^{35}S]Tom40 analyzed as in (A).

(D) Assembly of [^{35}S]Tom40 as described in (B). The area of the Tom40 assembly stages was quantified by autoradiography (SEM, n = 3 experiments). TOM, mature TOM complex; SAM-Ib and SAM-Ia, SAM import intermediates; Int-II, intermediate II.

(E) *In vitro* binding of the cyclic VDAC$_{257–279}$ TIM9·10 complexes, studied by NMR-based titration experiments, shows strongly reduced affinity in two Tim10 single point mutations (V29K, F33Q; blue) compared to wild-type TIM9·10 (black).

See also Figure S4.

and binding assays indicate that the affinity of the mutant TIM9·10 chaperones to the carrier precursors is significantly reduced, even though only three out of twelve tentacles of the TIM chaperone complex are affected by a single amino acid exchange.

TIM Chaperones Are Essential for the Transfer of β-Barrel Membrane Proteins

The TIM chaperones are also implicated in the import of β-barrel outer membrane proteins (Habib et al., 2005; Hoppins and Nargang, 2004; Wiedemann et al., 2004). Import of the most abundant β-barrel protein porin (mammalian VDAC) was monitored by blue native PAGE assembly of [^{35}S]Por1 (Figures 5A and 5B) and revealed defects in porin assembly for the TIM chaperone mutants. In addition, all assembly steps of the [^{35}S]Tom40 β-barrel biogenesis pathway, transfer to the SAM complex (intermediates Ia and Ib), generation of the membrane integral intermediate (Int-II), and assembly into the mature TOM complex, were affected in TIM chaperone mutants (Figures 5C and 5D). The analysis in the *tim8tim13*ΔΔ background demonstrated that the TIM chaperone system is also essential for the β-barrel membrane protein precursor transfer through the intermembrane space to the SAM complex similar to the role of the TIM chaperones for metabolite carrier biogenesis of the inner membrane. Moreover, the interaction of the VDAC$_{257–279}$ peptide to the TIM9·10 complex is reduced in case of *tim10* mutants (Figure 5E). Taken together, the in organello and *in vitro* analyses of the TIM chaperone mutants demonstrate that the hydrophobic TIM chaperone motif residues are crucial for the biogenesis of membrane proteins in both mitochondrial membranes. The quantitative comparison of the Tim10$_{L26Q}$ and *tim8tim13*ΔΔ mutants indicates that the biogenesis of the metabolite carrier Aac2 depends mainly on the TIM9·10 complex (Figures 4B and 4D). In contrast, the biogenesis of the β-barrel proteins porin and Tom40 are supported by both, the TIM8·13 and the TIM9·10 complexes (Figures 5B and 5D).

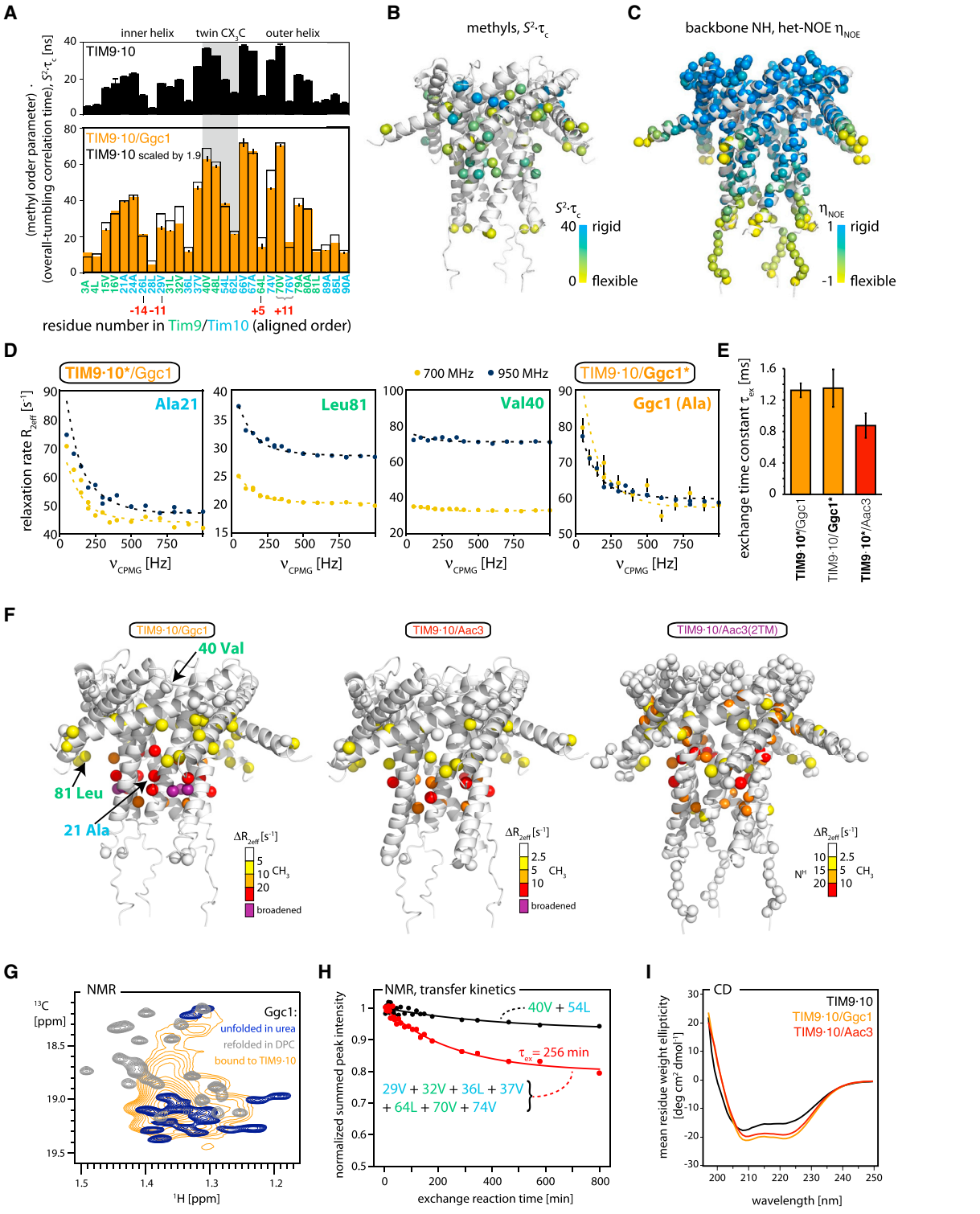

Figure 6. Dynamics of the TIM9·10/Carrier-Precursor Complex and Conformation of the Bound Precursor

(A) ps-to-ns dynamics probed by ALV methyl triple-quantum (3Q) relaxation experiments (Sun et al., 2011) showing the product of local order parameter and overall-tumbling correlation time constant, $S^2 \cdot \tau_c$, for apo (black) and Ggc1-bound TIM9·10 (orange). In the lower panel, the apo data have been multiplied by an overall factor (1.9) minimizing the offset of the two datasets. Error margins were determined from the spectral noise level, used in fitting the 3Q relaxation buildup curves; see STAR Methods.

(legend continued on next page)

Precursor Proteins Are Bound as a Dynamic Ensemble with Residual Secondary Structure

Having shown the essential role of the precursor protein binding motif *in vivo* and *in vitro*, we derived a complete description of the structure and dynamics of apo TIM9·10 and of the precursor protein-chaperone complex at atomic resolution. We first studied the flexibility (picosecond-to-nanosecond motions) of apo TIM9·10 using backbone ^{15}N and ALV $^{13}CH_3$ nuclear spin relaxation measurements and molecular dynamics (MD) simulation. The upper part of the inner and outer α helices is rigid, and the ''tentacles'' are increasingly flexible toward the N and C termini (Figures 6A–6C, S5A, and S5B). In the Ggc1-bound state, this pattern of intramolecular flexibility is well conserved. Figure 6A shows the profiles of the site-specific observable $S^2 \cdot \tau_c$, which is the product of the local order parameter (S^2) that describes the amplitude of motion of a given side chain and the correlation time of the overall molecular tumbling (τ_c) in apo (black) and Ggc1-bound states (orange). The residue-wise profiles of this parameter are in both states very similar, revealing that the local flexibility of the chaperone remains unchanged upon precursor protein binding. Together with the fact that apo and holo TIM9·10 NMR spectra are highly similar (Figures 1B and S1E–S1G), this data confirms that the hexameric TIM9·10 remains structurally unaltered. However, the apo and holo $S^2 \cdot \tau_c$ data differ by a uniform scaling factor of ~1.9, which points to a ~2-fold larger overall size of the TIM/precursor complex compared to apo TIM9·10 (see below).

We then probed the interaction dynamics of precursor proteins with TIM9·10 using Carr-Purcell-Meiboom-Gill (CPMG) relaxation-dispersion (RD) experiments (Korzhnev et al., 2004), which sense motions on microsecond-to-millisecond (μs-ms) timescales. When precursor protein (Aac3 or Ggc1) was bound to the chaperone, residues located in the binding cleft of TIM9·10 experienced μs-ms motions, as evidenced by non-flat RD profiles (Figure 6D); quantitative analysis shows that this motion occurred on a 0.8 ms (Aac3) to 1.3 ms (Ggc1) timescale (Figure 6E). In apo TIM9·10, these sites did not undergo ms motions (Figure S5C), establishing that the observed dynamics are directly linked to the chaperone/precursor protein interactions.

To gain further insight into this dynamic interaction, we studied the precursor protein conformation and dynamics. Figure 6G shows the NMR spectrum of the Ala methyl groups of Ggc1 bound to TIM9·10, and Figure S5D shows additional backbone amide and methyl spectra of Ggc1 and Aac3. The precursor protein spectra clearly differ from those of the fully unfolded state in urea, but also from the conformation of the refolded state in detergent where it forms predominantly α helices (Kurauskas et al., 2018). The broad resonance lines point to exchange dynamics between various conformations. To probe the presence of the precursor dynamics directly, we used CPMG NMR measurements of Ala and Ile methyl sites in Ggc1 bound to TIM9·10. While the low resolution of the methyl resonances, due to heterogeneity and dynamics, prohibits site-specific analysis, the CPMG data of the methyl resonances establish that the bound carrier undergoes motions on a timescale of ~1.3 ms (Figures 6D and 6E). This timescale matches quantitatively the one sensed by the residues in the binding cleft on the chaperone (Figure 6E), supporting the notion that we are observing intermolecular dynamics.

The dynamic process may correspond to (1) conformational rearrangements within the complex (''bound motion''), or (2) disruption and re-formation of the complex (''on/off''). The latter model would imply that precursor protein exists (transiently) freely in solution before rebinding to TIM. The existence of ''on/off'' dynamics can be probed by analyzing if precursor protein can be transferred between TIM chaperones. Transfer of the precursor was probed by mixing NMR-visible (labeled) apo-TIM9·10 with unlabeled holo-complex and following the NMR intensity drop (Figures S1E–S1G) associated to binding of precursor to the labeled chaperone. Figure 6H shows such intensity time traces, revealing that the transfer process occurs on a timescale of ~4 hr (Figure 6H), i.e., ~7 orders of magnitude longer than the observed ms dynamics, allowing us to unambiguously ascribe the observed ms dynamics to motions within the complex. The slow transfer of precursor protein and the long-time stability of our samples (weeks) suggest a high affinity.

The dynamic nature of the bound precursor protein and the associated broadening of NMR lines (Figure S5D) preclude site-specific analyses of the secondary structure at the residue level. To gain insight into the precursor protein conformation in the complex, we applied circular dichroism (CD) spectroscopy (Figure 6I). The apo TIM9·10 CD spectrum is in good agreement with the known hexameric structure consisting of α helices with flexible ends. When either Aac3 or Ggc1 are bound, the α-helical

(B) The data from (A) are plotted on the TIM9·10 structure.
(C) Local backbone dynamics probed by ^{1}H-^{15}N heteronuclear NOE measurements.
(D) ^{13}C methyl CPMG RD profiles in Ggc1-bound TIM9·10 for three representative residues of TIM9·10 (indicated with an arrow in F) and an Ala correlation peak of Ggc1, obtained at two magnetic-field strengths (700 MHz and 950 MHz ^{1}H Larmor frequencies). Non-flat profiles reveal ms dynamics. Error bars are based on spectral noise.
(E) Rate constant of the dynamic process obtained from a global fit of CPMG RD data of two independent TIM9·10/Ggc1 samples (orange), methyl-labeled either on TIM9·10 or Ggc1 (indicated by a star), and TIM9·10/Aac3 (red). Error bars were obtained from subjection the RD fit to a Monte Carlo procedure.
(F) Structural view of the amplitude of CPMG RD profiles, obtained from the difference of R_{2eff} at the lowest and highest CPMG frequency ν_{CPMG}. Residues for which data are shown in (D) are indicated by arrows.
(G) ^{1}H-^{13}C HMQC NMR spectra (Ala-CH_3) of Ggc1 in DPC detergent (folded), urea (unfolded) and bound to TIM9·10.
(H) Transfer kinetics of Aac3(2TM) from an unlabeled holo-TIM9·10 complex to added ALV-labeled apo-TIM9·10. Shown is the evolution of summed peak intensities of residues in the binding cleft (red), which have a strong intensity drop upon binding (Figure S1G) and on the top of TIM9·10 (black), less impacted by binding. The fitted decay rate constant is ~4.3 hr.
(I) Circular dichroism spectra of apo and precursor protein-loaded TIM9·10.
See Figure S5.

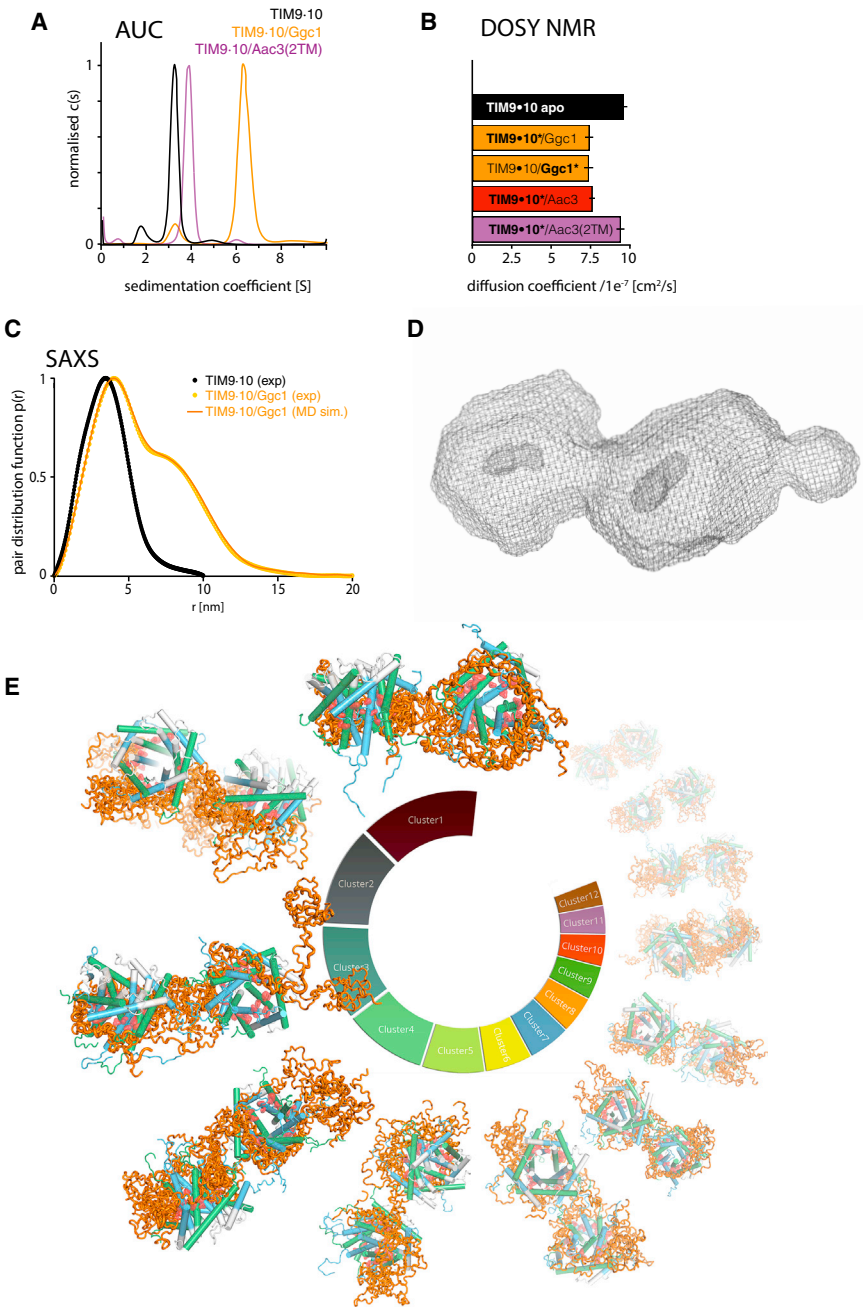

Figure 7. Architecture of the TIM/Metabolite Carrier Complexes

(A) Analytical ultracentrifugation profiles reveal the stoichiometry of TIM9·10/carrier precursor complexes.

(B) Translational diffusion coefficients of apo and holo TIM9·10 determined by diffusion ordered NMR. Error bars were from Monte Carlo analysis of the diffusion-data fit and the spectral noise level.

(C) Pair distance distributions obtained by taking an indirect Fourier transform of the experimental and back-predicted SAXS curves. The solid orange line shows the results from analyzing the back-calculated SAXS data from the ensemble of TIM9·10/Ggc1 conformations obtained from coarse-grained molecular dynamics. A view of the latter ensemble is provided in (E).

(D) Molecular envelope of TIM9·10/Ggc1 obtained from SAXS data.

(E) The most populated structures of the TIM9·10/Ggc1 complex from the coarse-grained molecular dynamics ensemble. The middle pie chart shows the population of the top 12 clusters which together occupy ~80% of the conformational space in total. The cartoon structures of these clusters are shown next to each chart.

See Figure S6.

signature becomes more pronounced. In principle, the additional α-helical structure in complex samples compared to apo-TIM may be ascribed to extended α-helical structure in the chaperone or α-helical structure of the bound precursor or both. Based on the fact that NMR spectra (Figures S1E–S1G) and internal dynamics (Figure 6A) of TIM9·10 remain unchanged upon precursor protein binding, we can exclude significant structural changes of the chaperone, allowing us to ascribe the increased α-helix CD signature to partial α-helical conformations of the bound precursor.

TIM Chaperones Hold Precursor Proteins in a Dynamic Elongated State

To gain an overall structural view of the complex, we determined the TIM/precursor protein stoichiometry from the sedimentation and translational diffusion coefficients of apo and holo complexes by analytical ultra-centrifugation (AUC) and diffusion-ordered NMR (DOSY). Our observations revealed consistently that the ~35 kDa carrier precursor protein recruits two TIM9·10 hexamers (Figures 7A and 7B). This 2:1 (TIM complex:precursor protein) stoichiometry is corroborated by the observation that the rotational diffusion correlation time of the holo complex, τ_c, is ~1.9-fold higher than the one of apo TIM9·10 (Figure 6A). Furthermore, analyses of band intensities on SDS-PAGE gels of 27 independent TIM9·10/Ggc1 samples further confirm the 2:1 molar ratio (Table S1).

We reasoned that the observed stoichiometry must be dependent on the precursor protein size and prepared complexes of a truncated construct of Aac3 comprising only two transmembrane segments, Aac3(2TM). Indeed, AUC and DOSY data revealed that this shorter precursor chain recruits only a single TIM9·10 hexamer (Figures 7A and 7B).

To gain a structural view of this complex, we turned to small-angle X-ray scattering (SAXS). The larger size of the complex,

compared to apo TIM9·10 is readily visible from the pair distribution function (Figure 7C) and the raw scattering data (Figures S6A–S6D). The envelope of the TIM9·10/Ggc1 complex (Figure 7D) shows two spherical densities matching two hexameric TIM chaperones. Two void volumes point to an unoccupied central cavity in each hexameric TIM, confirming that the central cavity is not involved in binding.

Data-Guided Molecular Dynamic Simulations Reveal a Dynamic Ensemble

We derived an ensemble description of this highly dynamic complex by integrating the information from all NMR and SAXS data into molecular dynamics simulations. Briefly, we constructed different conformations of the TIM9·10/Ggc1 complex by placing two TIM hexamers into the SAXS-envelope and placing the preprotein using the NMR data as restraints and performed coarse-grained molecular dynamics simulations to sample a large conformational space (Video S1). The conformational distribution was subsequently reweighted to match the SAXS data using an ensemble refinement method (Figures S6F–S6I). In the ensemble of structures (Figure 7E) the precursor protein is wrapped into the clamp-like binding sites of two hexameric modules, makes extensive contacts to the hydrophobic motif, and dynamically samples multiple conformations. The precursor protein adopts an elongated conformation holding the two chaperone hexamers in a modular ''bead-on-a-string'' architecture.

DISCUSSION

Chaperones of membrane proteins transport highly aggregation-prone polypeptides to their insertases. Premature release of these precursors would lead to protein aggregation with detrimental cellular consequences. Our study reveals that polypeptides belonging to classes of α-helical and β-barrel membrane proteins bind to the same binding cleft of the TIM chaperone. Conserved hydrophobic residues in this cleft are crucial for precursor protein binding and transfer through the intermembrane space. We further found that TIM chaperones comprising a single point mutation in Tim9 or Tim10 subunits are unable to hold precursor proteins, compromising yeast growth and viability. The binding site revealed in this study allows rationalizing why the premature stop at codon 80 of the human Tim8 analog, which prevents synthesis of leucine 81 corresponding to the position +15 of the hydrophobic motif, leads to import defects causing deafness dystonia syndrome, similarly to all larger truncations of the Tim8a protein (Koehler et al., 1999; Ujike et al., 2001).

Different precursors have a variable dependence on the TIM9·10 versus the TIM8·13 complex. While the intermembrane space transfer of the two major β-barrel proteins of the outer membrane porin and Tom40 depends on both ''transfer-chaperone'' complexes, binding and transfer of the metabolite carrier Aac2 depends predominantly on TIM9·10. Similarly, we observed a strong dependence of the carrier-like precursor Tim23 on the TIM9·10 complex, excluding a specific role of the TIM8·13 complex for Tim23 biogenesis (Paschen et al., 2000; Curran et al., 2002; Davis et al., 2007; Beverly et al., 2008).

Multiple Weak Binding Sites Enable High Affinity with Efficient Downstream Release

In addition to the requirement for tight binding, ''transfer-chaperones'' need to enable the release of their ''client'' protein in a conformation that enables downstream membrane insertion. Our integrated structural/dynamical data show that precursor proteins achieve their tight interaction to the chaperone by sampling a multitude of conformations within the binding cleft, with a lifetime of ~1 ms. This is orders of magnitude faster than the timescale required for the mitochondrial precursor protein import and assembly (seconds to min). The rapid interconversion of the precursor between a manifold of bound states points to the existence of multiple interactions, each individually weak, which together result in a high total affinity, as required for a stable transfer chaperone complex. The compatibility of high affinity with extreme mobility has been shown even for two intrinsically disordered proteins (Borgia et al., 2018).

We propose that the multiple weak and constantly reshuffling interactions allow efficient release to the insertase. According to the structural view provided here, parts of the precursor protein may transiently detach from the complex and engage with the insertase. The release of the remaining chain of the precursor protein upon membrane insertion can then proceed without significant free-energy barrier by gradually disengaging the multiple weak interactions (Burmann et al., 2013). While transfer of precursor from one TIM to another (no free-energy difference involved) takes ~4 hr, the release at the insertase is likely much faster due to the released free energy upon membrane insertion.

Transfer of Membrane Protein Precursors with Partial Secondary Structure

Currently, structural data on a membrane-protein/chaperone complex is available for the bacterial Skp chaperone encapsulating outer membrane protein (OMP) precursors in a central cavity in a highly dynamic random-coil-like compact state (Burmann et al., 2013; Schiffrin et al., 2016; Walton et al., 2009). Likewise, the periplasmic DegP protease/chaperone also harbors a compact conformation of β-barrel precursor proteins in the central cavity (Krojer et al., 2008). Our analysis of the eukaryotic TIM ''transfer-chaperone'' reveals a different principle for membrane-protein transfer, involving binding to the ''transfer-chaperone'' at specific equally spaced clamp-like binding motifs on the outside rather than in a central cavity. Furthermore, unlike the random-coil state of bacterial OMP precursors bound to Skp, full-length metabolite carrier precursors form likely partial α-helical secondary structure in a dynamic exchange of conformations. Likewise, formation of β-hairpin structure appears to be a prerequisite for mitochondrial outer-membrane precursor proteins to bind to TIM.

It has been shown that TOM and SAM form a supercomplex with a direct relay of β-barrel membrane protein precursors from the translocase to the insertase (Qiu et al., 2013). Therefore, stable full-length β-barrel membrane precursor protein/TIM chaperone complex formation is not required *in vivo*. The fact that complex formation under *in vitro* conditions was possible only for carrier preproteins but not β-barrel precursors suggests a lower binding affinity and may be related to the fact that

β-barrel biogenesis does not depend on external energy sources (Hagan et al., 2010), in contrast to the membrane-potential dependent insertion into the inner membrane. The β-hairpin conformation of the bound outer-membrane precursor, a prerequisite for binding to TIM, is ideally suited for β-barrel membrane protein insertion by the SAM complex (Höhr et al., 2018). The preformed β-hairpin conformation on the TIM "transfer-chaperones" suggests that the Sam50 POTRA domain is not essential for mitochondrial β-barrel protein biogenesis in contrast to the bacterial β-barrel biogenesis (Bos et al., 2007; Habib et al., 2007; Kutik et al., 2008), where the β-barrel precursor proteins are transported in an unstructured random-coil-like state (Burmann et al., 2013).

The chaperone-to-precursor stoichiometry depends on the length of the transported polypeptide. This modular architecture, reported also for other unrelated chaperones (Saio et al., 2014; Schiffrin et al., 2016), allows the TIM system to handle the wide range of incoming precursor chains, from ~17 kDa (Tim17) to 50 kDa (Sal1, Sam50).

TIM "Transfer-Chaperones" Mimic Co-translational Membrane Insertion

Taken together, the TIM "transfer-chaperones" provide multiple clamp-like binding sites to hold the precursors in an elongated conformation and to keep the hydrophobic transmembrane domains apart from each other. The TIM chaperones have the remarkable property to bind precursors containing preformed elements of both secondary structure classes, which provides an ideal prerequisite for subsequent membrane insertion. The segmental transfer mechanism maintains the precursor in a translocation competent "nascent chain-like" conformation and enables efficient translocation by the membrane insertion machineries. The mitochondrial TIM "transfer-chaperone" system thus mimics elements of co-translational membrane insertion, providing a paradigm for chaperone-guided membrane protein insertion in ribosome-free compartments such as the mitochondrial and chloroplast intermembrane spaces.

STAR★METHODS

Detailed methods are provided in the online version of this paper and include the following:

- KEY RESOURCES TABLE
- CONTACT FOR REAGENT AND RESOURCE SHARING
- EXPERIMENTAL MODEL AND SUBJECT DETAILS
- METHODS DETAILS
  - Protein constructs of TIM9·10 and carrier precursor proteins used for *in vitro* experiments
  - Buffers mentioned in the descriptions below
  - Cloning, expression and purification of TIM9·10
  - Expression and purification of TIM9·10 substrates Ggc1, Ggc1-C222S, Ggc1-C222S/C8Q, Aac3 and Aac3(2TM)
  - Isotope labeling
  - Site-specific spin-labeling of scGGC1
  - Production of chaperone-precursor protein complexes
  - Cell-free expression of Ggc1 in the absence or presence of TIM9·10
  - Analytical ultracentrifugation
  - Circular dichroism spectroscopy
  - NMR spectroscopy
  - VDAC peptide titration
  - Cross-linking of VDAC peptides to TIM9·10
  - Small-angle X-ray scattering data collection and analysis
  - Molecular dynamics simulations
  - Workflow of the ensemble refinement using SAXS data
  - Yeast handling and growth conditions
  - Isolation of mitochondria
  - Site-directed mutagenesis
  - Gel electrophoresis and western blotting
  - *In vitro* transcription and translation
  - *In vitro* import into mitochondria
  - Membrane potential assessment
- QUANTIFICATION AND STATISTICAL ANALYSIS
  - General considerations about quantitative analysis of NMR data
  - Diffusion ordered NMR spectroscopy
  - Methyl order parameter measurements from relaxation-violated coherence transfer NMR
  - CPMG experiments
  - *In vitro* import experiments
- DATA AND SOFTWARE AVAILABILITY

SUPPLEMENTAL INFORMATION

Supplemental Information includes six figures, four tables, and one video and can be found with this article online at https://doi.org/10.1016/j.cell.2018.10.039.

ACKNOWLEDGMENTS

We thank Nikolaus Pfanner, Vilius Kurauskas, Sebastian Hiller, and Sandro Bottaro for discussions and Aline Le Roy and Christine Ebel for AUC experiments. This work was supported by the European Research Council (StG 311318 and CoG 648235), the Sonderforschungsbereich 1140, the Excellence initiative of the German federal and state governments (EXC 294 BIOSS and GSC-4 Spemann Graduate School), the BRAINSTRUC initiative from the Lundbeck Foundation, and the Deutsche Forschungsgemeinschaft (RA1028/8-1 to D.R.). We thank the ESRF for beamtime at BM29. This work used the high-field NMR and EM facilities at the Grenoble Instruct-ERIC Center (ISBG; UMS 3518 CNRS CEA-UJF-EMBL) with support from FRISBI (ANR-10-INSB-05-02) and GRAL (ANR-10-LABX-49-01) within the Grenoble Partnership for Structural Biology. Work included in this study has also been performed in partial fulfillment of the requirements for the doctoral theses of K.W. (University Grenoble Alpes) and C.L. (University of Freiburg).

AUTHOR CONTRIBUTIONS

K.W. and P.S. initiated this study. K.W. performed all *in vitro*/structural biology experiments (sample preparation, NMR, SAXS) and analyzed data. C.L. performed cloning experiments (with C.S. and L.M.), characterized the mutants, and performed mitochondrial import experiments (with C.S. and B.S). A.H. and B.B. prepared samples of TIM, Ggc1, Aac3, and complexes thereof. Y.W. performed and analyzed molecular dynamics simulations. T.J. performed cross-linking experiments of TIM9·10 with VDAC peptides, which were synthesized by H.K. M.B. assisted in the collection of SAXS data and performed

SAXS data processing. K.L.-L., D.R., N.W., and P.S. conceived experiments, interpreted results, and supervised this work. K.W., C.L., N.W., and P.S. wrote the paper.

DECLARATION OF INTERESTS

The authors declare no competing interests.

Received: March 19, 2018
Revised: August 16, 2018
Accepted: October 15, 2018
Published: November 15, 2018

REFERENCES

Abraham, M.J., Murtola, T., Schulz, R., Páll, S., Smith, J.C., Hess, B., and Lindahl, E. (2015). GROMACS: High performance molecular simulations through multi-level parallelism from laptops to supercomputers. SoftwareX *1*, 19–25.

Ashiotis, G., Deschildre, A., Nawaz, Z., Wright, J.P., Karkoulis, D., Picca, F.E., and Kieffer, J. (2015). The fast azimuthal integration Python library: *pyFAI*. J. Appl. Cryst. *48*, 510–519.

Baker, M.J., Webb, C.T., Stroud, D.A., Palmer, C.S., Frazier, A.E., Guiard, B., Chacinska, A., Gulbis, J.M., and Ryan, M.T. (2009). Structural and functional requirements for activity of the Tim9-Tim10 complex in mitochondrial protein import. Mol. Biol. Cell *20*, 769–779.

Baker, M.J., Mooga, V.P., Guiard, B., Langer, T., Ryan, M.T., and Stojanovski, D. (2012). Impaired folding of the mitochondrial small TIM chaperones induces clearance by the i-AAA protease. J. Mol. Biol. *424*, 227–239.

Beverly, K.N., Sawaya, M.R., Schmid, E., and Koehler, C.M. (2008). The Tim8-Tim13 complex has multiple substrate binding sites and binds cooperatively to Tim23. J. Mol. Biol. *382*, 1144–1156.

Borgia, A., Borgia, M.B., Bugge, K., Kissling, V.M., Heidarsson, P.O., Fernandes, C.B., Sottini, A., Soranno, A., Buholzer, K.J., Nettels, D., et al. (2018). Extreme disorder in an ultrahigh-affinity protein complex. Nature *555*, 61–66.

Bos, M.P., Robert, V., and Tommassen, J. (2007). Functioning of outer membrane protein assembly factor Omp85 requires a single POTRA domain. EMBO Rep. *8*, 1149–1154.

Bottaro, S., Bussi, G., Kennedy, S.D., Turner, D.H., and Lindorff-Larsen, K. (2017). Conformational Ensemble of RNA Oligonucleotides from Integrating NMR and Molecular Simulations. Sci. Adv. *4*, eaar8521.

Brennich, M.E., Kieffer, J., Bonamis, G., De Maria Antolinos, A., Hutin, S., Pernot, P., and Round, A. (2016). Online data analysis at the ESRF bioSAXS beamline, BM29. J. Appl. Cryst. *49*, 203–212.

Brennich, M.E., Round, A.R., and Hutin, S. (2017). Online size-exclusion and ion-exchange chromatography on a SAXS beamline. J. Vis. Exp. (119), 54861.

Burmann, B.M., Wang, C., and Hiller, S. (2013). Conformation and dynamics of the periplasmic membrane-protein-chaperone complexes OmpX-Skp and tOmpA-Skp. Nat. Struct. Mol. Biol. *20*, 1265–1272.

Chacinska, A., Pfannschmidt, S., Wiedemann, N., Kozjak, V., Sanjuán Szklarz, L.K., Schulze-Specking, A., Truscott, K.N., Guiard, B., Meisinger, C., and Pfanner, N. (2004). Essential role of Mia40 in import and assembly of mitochondrial intermembrane space proteins. EMBO J. *23*, 3735–3746.

Clementi, C., Nymeyer, H., and Onuchic, J.N. (2000). Topological and energetic factors: what determines the structural details of the transition state ensemble and "en-route" intermediates for protein folding? An investigation for small globular proteins. J. Mol. Biol. *298*, 937–953.

Curran, S.P., Leuenberger, D., Oppliger, W., and Koehler, C.M. (2002). The Tim9p-Tim10p complex binds to the transmembrane domains of the ADP/ATP carrier. EMBO J. *21*, 942–953.

Daura, X., Gademann, K., Jaun, B., Seebach, D., van Gunsteren, W.F., and Mark, A.E. (1999). Peptide folding: when simulation meets experiment. Angew. Chem. Int. *38*, 236–240.

Davis, A.J., Alder, N.N., Jensen, R.E., and Johnson, A.E. (2007). The Tim9p/10p and Tim8p/13p complexes bind to specific sites on Tim23p during mitochondrial protein import. Mol. Biol. Cell *18*, 475–486.

Delaglio, F., Grzesiek, S., Vuister, G.W., Zhu, G., Pfeifer, J., and Bax, A. (1995). NMRPipe: a multidimensional spectral processing system based on UNIX pipes. J. Biomol. NMR *6*, 277–293.

Didenko, T., Boelens, R., and Rüdiger, S.G.D. (2011). 3D DOSY-TROSY to determine the translational diffusion coefficient of large protein complexes. Protein Eng. Des. Sel. *24*, 99–103.

Dolezal, P., Likic, V., Tachezy, J., and Lithgow, T. (2006). Evolution of the molecular machines for protein import into mitochondria. Science *313*, 314–318.

Favier, A., and Brutscher, B. (2011). Recovering lost magnetization: polarization enhancement in biomolecular NMR. J. Biomol. NMR *49*, 9–15.

Franke, D., Petoukhov, M.V., Konarev, P.V., Panjkovich, A., Tuukkanen, A., Mertens, H.D.T., Kikhney, A.G., Hajizadeh, N.R., Franklin, J.M., Jeffries, C.M., and Svergun, D.I. (2017). *ATSAS 2.8*: a comprehensive data analysis suite for small-angle scattering from macromolecular solutions. J. Appl. Cryst. *50*, 1212–1225.

Haan, C., and Behrmann, I. (2007). A cost effective non-commercial ECL-solution for Western blot detections yielding strong signals and low background. J. Immunol. Methods *318*, 11–19.

Habib, S.J., Waizenegger, T., Lech, M., Neupert, W., and Rapaport, D. (2005). Assembly of the TOB complex of mitochondria. J. Biol. Chem. *280*, 6434–6440.

Habib, S.J., Waizenegger, T., Niewienda, A., Paschen, S.A., Neupert, W., and Rapaport, D. (2007). The N-terminal domain of Tob55 has a receptor-like function in the biogenesis of mitochondrial β-barrel proteins. J. Cell Biol. *176*, 77–88.

Hagan, C.L., Kim, S., and Kahne, D. (2010). Reconstitution of outer membrane protein assembly from purified components. Science *328*, 890–892.

Höhr, A.I.C., Lindau, C., Wirth, C., Qiu, J., Stroud, D.A., Kutik, S., Guiard, B., Hunte, C., Becker, T., Pfanner, N., et al. (2018). Membrane protein insertion through a mitochondrial βembrane prote. Science *359*, eaah6834.

Hoppins, S.C., and Nargang, F.E. (2004). The Tim8-Tim13 complex of Neurospora crassa functions in the assembly of proteins into both mitochondrial membranes. J. Biol. Chem. *279*, 12396–12405.

Hummer, G., and Köfinger, J. (2015). Bayesian ensemble refinement by replica simulations and reweighting. J. Chem. Phys. *143*, 243150.

Hynson, R.M.G., Duff, A.P., Kirby, N., Mudie, S., and Lee, L.K. (2015). Differential ultracentrifugation coupled to small-angle X-ray scattering on macromolecular complexes. J. Appl. Cryst. *48*, 769–775.

Janke, C., Magiera, M.M., Rathfelder, N., Taxis, C., Reber, S., Maekawa, H., Moreno-Borchart, A., Doenges, G., Schwob, E., Schiebel, E., and Knop, M. (2004). A versatile toolbox for PCR-based tagging of yeast genes: new fluorescent proteins, more markers and promoter substitution cassettes. Yeast *21*, 947–962.

Jores, T., Klinger, A., Groß, L.E., Kawano, S., Flinner, N., Duchardt-Ferner, E., Wöhnert, J., Kalbacher, H., Endo, T., Schleiff, E., and Rapaport, D. (2016). Characterization of the targeting signal in mitochondrial β-barrel proteins. Nat. Commun. *7*, 12036.

Kerscher, O., Holder, J., Srinivasan, M., Leung, R.S., and Jensen, R.E. (1997). The Tim54p-Tim22p complex mediates insertion of proteins into the mitochondrial inner membrane. J. Cell Biol. *139*, 1663–1675.

Knight, C.J., and Hub, J.S. (2015). WAXSiS: a web server for the calculation of SAXS/WAXS curves based on explicit-solvent molecular dynamics. Nucleic Acids Res. *43* (W1), W225-30.

Koehler, C.M., Jarosch, E., Tokatlidis, K., Schmid, K., Schweyen, R.J., and Schatz, G. (1998). Import of mitochondrial carriers mediated by essential proteins of the intermembrane space. Science *279*, 369–373.

Koehler, C.M., Leuenberger, D., Merchant, S., Renold, A., Junne, T., and Schatz, G. (1999). Human deafness dystonia syndrome is a mitochondrial disease. Proc. Natl. Acad. Sci. USA *96*, 2141–2146.

Korzhnev, D.M., Kloiber, K., Kanelis, V., Tugarinov, V., and Kay, L.E. (2004). Probing slow dynamics in high molecular weight proteins by methyl-TROSY NMR spectroscopy: application to a 723-residue enzyme. J. Am. Chem. Soc. *126*, 3964–3973.

Krojer, T., Sawa, J., Schäfer, E., Saibil, H.R., Ehrmann, M., and Clausen, T. (2008). Structural basis for the regulated protease and chaperone function of DegP. Nature *453*, 885–890.

Kupce, E., Boyd, J., and Campbell, I.D. (1995). Short selective pulses for biochemical applications. J. Magn. Reson. B. *106*, 300–303.

Kurauskas, V., Hessel, A., Ma, P., Lunetti, P., Weinhäupl, K., Imbert, L., Brutscher, B., King, M.S., Sounier, R., Dolce, V., et al. (2018). How detergent impacts membrane proteins: atomic-level views of mitochondrial carriers in dodecylphosphocholine. J. Phys. Chem. Lett. *9*, 933–938.

Kutik, S., Stojanovski, D., Becker, L., Becker, T., Meinecke, M., Krüger, V., Prinz, C., Meisinger, C., Guiard, B., Wagner, R., et al. (2008). Dissecting membrane insertion of mitochondrial β-barrel proteins. Cell *132*, 1011–1024.

Lindorff-Larsen, K., Piana, S., Palmo, K., Maragakis, P., Klepeis, J.L., Dror, R.O., and Shaw, D.E. (2010). Improved side-chain torsion potentials for the Amber ff99SB protein force field. Proteins *78*, 1950–1958.

Lionaki, E., de Marcos Lousa, C., Baud, C., Vougioukalaki, M., Panayotou, G., and Tokatlidis, K. (2008). The essential function of Tim12 in vivo is ensured by the assembly interactions of its C-terminal domain. J. Biol. Chem. *283*, 15747–15753.

Martín-Benito, J., Gómez-Reino, J., Stirling, P.C., Lundin, V.F., Gómez-Puertas, P., Boskovic, J., Chacón, P., Fernández, J.J., Berenguer, J., Leroux, M.R., and Valpuesta, J.M. (2007). Divergent substrate-binding mechanisms reveal an evolutionary specialization of eukaryotic prefoldin compared to its archaeal counterpart. Structure *15*, 101–110.

Mesecke, N., Terziyska, N., Kozany, C., Baumann, F., Neupert, W., Hell, K., and Herrmann, J.M. (2005). A disulfide relay system in the intermembrane space of mitochondria that mediates protein import. Cell *121*, 1059–1069.

Miyazawa, S., and Jernigan, R.L. (1996). Residue-residue potentials with a favorable contact pair term and an unfavorable high packing density term, for simulation and threading. J. Mol. Biol. *256*, 623–644.

Morgenstern, M., Stiller, S.B., Lübbert, P., Peikert, C.D., Dannenmaier, S., Drepper, F., Weill, U., Höß, P., Feuerstein, R., Gebert, M., et al. (2017). Definition of a high-confidence mitochondrial proteome at quantitative scale. Cell Rep. *19*, 2836–2852.

Neupert, W., and Herrmann, J.M. (2007). Translocation of proteins into mitochondria. Annu. Rev. Biochem. *76*, 723–749.

Paschen, S.A., Rothbauer, U., Kaldi, K., Bauer, M.F., Neupert, W., and Brunner, M. (2000). The role of the TIM8-13 complex in the import of Tim23 into mitochondria. EMBO J *19*, 6392–6400.

Paschen, S.A., Waizenegger, T., Stan, T., Preuss, M., Cyrklaff, M., Hell, K., Rapaport, D., and Neupert, W. (2003). Evolutionary conservation of biogenesis of β-barrel membrane proteins. Nature *426*, 862–866.

Pernot, P., Round, A., Barrett, R., De Maria Antolinos, A., Gobbo, A., Gordon, E., Huet, J., Kieffer, J., Lentini, M., Mattenet, M., et al. (2013). Upgraded ESRF BM29 beamline for SAXS on macromolecules in solution. J. Synchrotron Radiat. *20*, 660–664.

Petoukhov, M.V., Franke, D., Shkumatov, A.V., Tria, G., Kikhney, A.G., Gajda, M., Gorba, C., Mertens, H.D.T., Konarev, P.V., and Svergun, D.I. (2012). New developments in the *ATSAS* program package for small-angle scattering data analysis. J. Appl. Cryst. *45*, 342–350.

Qiu, J., Wenz, L.-S., Zerbes, R.M., Oeljeklaus, S., Bohnert, M., Stroud, D.A., Wirth, C., Ellenrieder, L., Thornton, N., Kutik, S., et al. (2013). Coupling of mitochondrial import and export translocases by receptor-mediated supercomplex formation. Cell *154*, 596–608.

Rehling, P., Model, K., Brandner, K., Kovermann, P., Sickmann, A., Meyer, H.E., Kühlbrandt, W., Wagner, R., Truscott, K.N., and Pfanner, N. (2003). Protein insertion into the mitochondrial inner membrane by a twin-pore translocase. Science *299*, 1747–1751.

Riek, R., Wider, G., Pervushin, K., and Wüthrich, K. (1999). Polarization transfer by cross-correlated relaxation in solution NMR with very large molecules. Proc. Natl. Acad. Sci. USA *96*, 4918–4923.

Rotkiewicz, P., and Skolnick, J. (2008). Fast procedure for reconstruction of full-atom protein models from reduced representations. J. Comput. Chem. *29*, 1460–1465.

Round, A., Felisaz, F., Fodinger, L., Gobbo, A., Huet, J., Villard, C., Blanchet, C.E., Pernot, P., McSweeney, S., Roessle, M., et al. (2015). BioSAXS Sample Changer: a robotic sample changer for rapid and reliable high-throughput X-ray solution scattering experiments. Acta Crystallogr. D Biol. Crystallogr. *71*, 67–75.

Ryan, M.T., Müller, H., and Pfanner, N. (1999). Functional staging of ADP/ATP carrier translocation across the outer mitochondrial membrane. J. Biol. Chem. *274*, 20619–20627.

Saio, T., Guan, X., Rossi, P., Economou, A., and Kalodimos, C.G. (2014). Structural basis for protein antiaggregation activity of the trigger factor chaperone. Science *344*, 1250494.

Schanda, P., Forge, V., and Brutscher, B. (2006). HET-SOFAST NMR for fast detection of structural compactness and heterogeneity along polypeptide chains. Magn. Reson. Chem. *44*, S177–S184.

Schiffrin, B., Calabrese, A.N., Devine, P.W.A., Harris, S.A., Ashcroft, A.E., Brockwell, D.J., and Radford, S.E. (2016). Skp is a multivalent chaperone of outer-membrane proteins. Nat. Struct. Mol. Biol. *23*, 786–793.

Schneidman-Duhovny, D., Hammel, M., Tainer, J.A., and Sali, A. (2013). Accurate SAXS profile computation and its assessment by contrast variation experiments. Biophys. J. *105*, 962–974.

Sirrenberg, C., Bauer, M.F., Guiard, B., Neupert, W., and Brunner, M. (1996). Import of carrier proteins into the mitochondrial inner membrane mediated by Tim22. Nature *384*, 582–585.

Sirrenberg, C., Endres, M., Fölsch, H., Stuart, R.A., Neupert, W., and Brunner, M. (1998). Carrier protein import into mitochondria mediated by the intermembrane proteins Tim10/Mrs11 and Tim12/Mrs5. Nature *391*, 912–915.

Stojanovski, D., Pfanner, N., and Wiedemann, N. (2007). Import of proteins into mitochondria. Methods Cell Biol. *80*, 783–806.

Sun, H., Kay, L.E., and Tugarinov, V. (2011). An optimized relaxation-based coherence transfer NMR experiment for the measurement of side-chain order in methyl-protonated, highly deuterated proteins. J. Phys. Chem. B *115*, 14878–14884.

Svergun, D.I. (1992). Determination of the regularization parameter in indirect-transform methods using perceptual criteria. J. Appl. Cryst. *25*, 495–503.

Tribello, G.A., Bonomi, M., Branduardi, D., Camilloni, C., and Bussi, G. (2014). PLUMED 2: new feathers for an old bird. Comput. Phys. Commun. *185*, 604–613.

Truscott, K.N., Wiedemann, N., Rehling, P., Müller, H., Meisinger, C., Pfanner, N., and Guiard, B. (2002). Mitochondrial import of the ADP/ATP carrier: the essential TIM complex of the intermembrane space is required for precursor release from the TOM complex. Mol. Cell. Biol. *22*, 7780–7789.

Ujike, H., Tanabe, Y., Takehisa, Y., Hayabara, T., and Kuroda, S. (2001). A family with X-linked dystonia-deafness syndrome with a novel mutation of the DDP gene. Arch. Neurol. *58*, 1004–1007.

Vergnolle, M.A., Baud, C., Golovanov, A.P., Alcock, F., Luciano, P., Lian, L.-Y., and Tokatlidis, K. (2005). Distinct domains of small Tims involved in subunit interaction and substrate recognition. J. Mol. Biol. *351*, 839–849.

Vial, S., Lu, H., Allen, S., Savory, P., Thornton, D., Sheehan, J., and Tokatlidis, K. (2002). Assembly of Tim9 and Tim10 into a functional chaperone. J. Biol. Chem. *277*, 36100–36108.

Vranken, W.F., Boucher, W., Stevens, T.J., Fogh, R.H., Pajon, A., Llinas, M., Ulrich, E.L., Markley, J.L., Ionides, J., and Laue, E.D. (2005). The CCPN data model for NMR spectroscopy: development of a software pipeline. Proteins *59*, 687–696.

Walton, T.A., Sandoval, C.M., Fowler, C.A., Pardi, A., and Sousa, M.C. (2009). The cavity-chaperone Skp protects its substrate from aggregation but allows independent folding of substrate domains. Proc. Natl. Acad. Sci. USA *106*, 1772–1777.

Wang, Y., Gan, L., Wang, E., and Wang, J. (2013). Exploring the dynamic functional landscape of adenylate kinase modulated by substrates. J. Chem. Theory Comput. *9*, 84–95.

Wang, Y., Tang, C., Wang, E., and Wang, J. (2014). PolyUbiquitin chain linkage topology selects the functions from the underlying binding landscape. PLoS Comput. Biol. *10*, e1003691.

Webb, B., and Sali, A. (2014). Protein structure modeling with MODELLER. Protein Structure Prediction (Springer), pp. 1–15.

Webb, C.T., Gorman, M.A., Lazarou, M., Ryan, M.T., and Gulbis, J.M. (2006). Crystal structure of the mitochondrial chaperone TIM9.10 reveals a six-bladed α-propeller. Mol. Cell *21*, 123–133.

Wiedemann, N., and Pfanner, N. (2017). Mitochondrial machineries for protein import and assembly. Annu. Rev. Biochem. *86*, 685–714.

Wiedemann, N., Kozjak, V., Chacinska, A., Schönfisch, B., Rospert, S., Ryan, M.T., Pfanner, N., and Meisinger, C. (2003). Machinery for protein sorting and assembly in the mitochondrial outer membrane. Nature *424*, 565–571.

Wiedemann, N., Truscott, K.N., Pfannschmidt, S., Guiard, B., Meisinger, C., and Pfanner, N. (2004). Biogenesis of the protein import channel Tom40 of the mitochondrial outer membrane: intermembrane space components are involved in an early stage of the assembly pathway. J. Biol. Chem. *279*, 18188–18194.

STAR★METHODS

KEY RESOURCES TABLE

REAGENT or RESOURCE	SOURCE	IDENTIFIER
Antibodies		
Rabbit polyclonal anti-Tom70 (GR657-4)	Nils Wiedemann	N/A
Rabbit polyclonal anti-Tom40 (168-4)	Nils Wiedemann	N/A
Rabbit polyclonal anti-Tom22 (GR3227-2)	Nils Wiedemann	N/A
Rabbit polyclonal anti-Tom5 (GR3420-7)	Nils Wiedemann	N/A
Rabbit polyclonal anti-Om45 (GR1390-4)	Nils Wiedemann	N/A
Rabbit polyclonal anti-Sam50 (312-7)	Nils Wiedemann	N/A
Rabbit polyclonal anti-Por1 (GR3622-3)	Nils Wiedemann	N/A
Rabbit polyclonal anti-Sdh1 (GR1849-3)	Nils Wiedemann	N/A
Rabbit polyclonal anti-Ssc1 (119-5)	Nils Wiedemann	N/A
Rabbit polyclonal anti-Mdj1 (GR1839-7)	Nils Wiedemann	N/A
Rabbit polyclonal anti-Tim54 (GR2012-5)	Nils Wiedemann	N/A
Rabbit polyclonal anti-Tim23 (GR3878-4)	Nils Wiedemann	N/A
Rabbit polyclonal anti-Tim22 (164-8)	Nils Wiedemann	N/A
Rabbit polyclonal anti-Tim13 (GR2044-5)	Nils Wiedemann	N/A
Rabbit polyclonal anti-Tim10 (217-8)	Nils Wiedemann	N/A
Rabbit polyclonal anti-Tim9 (GR2013-7)	Nils Wiedemann	N/A
Rabbit polyclonal anti-Aac2 (GR3617-7)	Nils Wiedemann	N/A
Rabbit polyclonal anti-Dic1 (GR2055-KB)	Nils Wiedemann	N/A
Rabbit polyclonal anti-Yhm2 (GR3053-5)	Nils Wiedemann	N/A
Rabbit polyclonal anti-Cox1 (GR1538-4)	Nils Wiedemann	N/A
Rabbit polyclonal anti-Tim12 (GR905-AP)	Nils Wiedemann	N/A
Anti-Rabbit IgG (whole molecule)-peroxidase, antibody produced in goat	Sigma-Aldrich	Cat. #A6154; RRID:AB_258284
Monoclonal Anti-polyHistidine–Peroxidase antibody produced in mouse	Sigma-Aldrich	Cat. #A7058; RRID:AB_258326
Bacterial and Virus Strains		
XL-1 Blue *Escherichia coli*	Stratagene	Cat. #200158
SHuffle® T7 Competent Cells	NEB	Cat. #C3026J
BL21(DE3) Chemically Competent Cells	Sigma-Aldrich	Cat. #CMC0014
XL1-Blue Supercompetent Cells	Stratagene/Agilent	Cat. #200236
Chemicals, Peptides, and Recombinant Proteins		
Q5 High-Fidelity DNA Polymerase	NEB	Cat. #M0492S
DPNI	NEB	Cat. #R0176S
Nourseothricin Dihydrogensulfat	Roth	Cat. #3011.3
Hygromycin B	Roth	Cat. #CP13.3
Polyethylene glycol (PEG4000)	Merck Millipore	Cat. #1097270100
SC amino acids without tryptophan	MP Biomedicals	Cat. #4511-022
SC amino acids without uracil	MP Biomedicals	Cat. #4511-222
Yeast nitrogen base without amino acids	Becton Dickinson	Cat. #291920
Agar	Becton Dickinson	Cat. #214030
Glucose	Roth	Cat. #6780.1
5-Fluoroorotic acid (5FOA)	Melford	Cat. #F10501-10.0
Uracil	Fluka Analytical	Cat. #94220

(*Continued on next page*)

Continued

REAGENT or RESOURCE	SOURCE	IDENTIFIER
Yeast extract	Becton Dickinson	Cat. #212720
Bacto peptone	Becton Dickinson	Cat. #211820
Glycerol	Honeywell	Cat. #G7757-1GA
Zymolyase 20T	Nacalai tesque INC.	Cat. #07663-91
Digitonin WS	MATRIX BioScience	Cat. #60105
^{35}S-methionine	Perkin Elmer	Cat. #NEG009T005MC
3,3′-dipropylthiadicarbocyanine iodide (DiSC3)	Invitrogen	Cat. #D306
Cyclic VDAC beta hairpin peptide	Jores et al., 2016	Doron Rapaport
Linear VDAC beta hairpin peptide	Jores et al., 2016	Doron Rapaport
Ala^{β} CH_3 labeling reagents	NMR-Bio, http://nmr-bio.com	SLAM-A^{β} kit
Leu^{proS} + Val^{proS} CH_3 labeling reagents	NMR-Bio, http://nmr-bio.com	DLAM-^{LVproS} kit
Ala^{β} + Ile^{β} CH_3 labeling reagents	NMR-Bio, http://nmr-bio.com	DLAM-$A^{\beta}/I^{\delta1}$ kit
(1-oxyl-2,2,5,5-tetramethyl-Δ3-pyrroline-3-methyl)-methanethiosulfonate)	Toronto Research Chemicals	Cat. #O875000
Critical Commercial Assays		
TNT SP6 quick coupled kit	Promega	Cat. #L2080
Rabbit Reticulocyte Lysate System	Promega	Cat. #L4540
mMESSAGE mMACHINE SP6 kit	Invitrogene	Cat. #AM1340
Deposited Data		
TIM9•10 NMR assignment	BioMagResBank, http://www.bmrb.wisc.edu	BMRB: 27052
SAXS data and complex models from MD	SASBDB, https://www.sasbdb.org	SASDEF2 (TIM9·10) SASDEG2 (TIM9·10/Ggc1)
CPMG relaxation dispersion data	Mendeley data	https://doi.org/10.17632/k6d77j8vzp.1
Chemical-shift perturbation of Tim10-mutants F33Q and V29K	Mendeley data	http://dx.doi.org/10.17632/c9bp4dt5bz.1
Methyl order parameter measurements from relaxation-violated coherence transfer NMR	Mendeley data	https://doi.org/10.17632/cn9j8wtndj.1
Experimental Models: Organisms/Strains		
YPH499 *MATa ura3-52 lys2-801_amber ade2-101_ochre trp1-Δ63 his3-Δ200 leu2-Δ1*	LGC Standards/ATCC	http://www.atcc.org/?geo_country=us
YPH499 *tim9::ade2* [Yep352-MET25pr-Tim9-CYC1t]	Baker et al., 2009	yNW-5080
YPH499 *tim10::ade2* [Yep352-MET25pr-Tim10-CYC1t]	Truscott et al., 2002	yNW-5081
YPH499 *tim9::ade2 tim8::natNT2 tim13::hphNT1* [Yep352-MET25pr-Tim9-CYC1t]	This paper	yNW-5082
YPH499 *tim10::ade2 tim8::natNT2 tim13:: hphNT1* [Yep352-MET25pr-Tim10-CYC1t]	This paper	yNW-5083
YPH499 *tim9::ade2* [pFL39-Tim9]	This paper	yNW-5117
YPH499 *tim10::ade2* [pFL39-Tim10]	This paper	yNW-5118
YPH499 *tim9::ade2 tim8::natNT2 tim13::hphNT1* [pFL39-Tim9]	This paper	yNW-5119
YPH499 *tim10::ade2 tim8::natNT2 tim13::hphNT1* [pFL39-Tim10]	This paper	yNW-5084
YPH499 *tim10::ade2 tim8::natNT2 tim13::hphNT1* [pFL39-Tim10$_{L26Q}$]	This paper	yNW-5206
YPH499 *tim10::ade2 tim8::natNT2 tim13::hphNT1* [pFL39-Tim10$_{V29S}$]	This paper	yNW-5085
YPH499 *tim10::ade2 tim8::natNT2 tim13::hphNT1* [pFL39-Tim10$_{M32S}$]	This paper	yNW-5086

(*Continued on next page*)

Continued

REAGENT or RESOURCE	SOURCE	IDENTIFIER
YPH499 *tim10::ade2 tim8::natNT2 tim13::hphNT1* [pFL39-Tim10$_{F33Q}$]	This paper	yNW-5087
YPH499 *tim10::ade2 tim8::natNT2 tim13::hphNT1* [pFL39-Tim10$_{V76S}$]	This paper	yNW-5090
YPH499 *tim10::ade2 tim8::natNT2 tim13::hphNT1* [pFL39-Tim10$_{F70S}$]	This paper	yNW-5207
YPH499 *tim9::ade2 tim8::natNT2 tim13::hphNT1* [pFL39-Tim9$_{M21K}$]	This paper	yNW-5094
YPH499 *tim9::ade2 tim8::natNT2 tim13::hphNT1* [pFL39-Tim9$_{F24K}$]	This paper	yNW-5096
YPH499 *tim9::ade2 tim8::natNT2 tim13::hphNT1* [pFL39-Tim9$_{L27K}$]	This paper	yNW-5208
YPH499 *tim9::ade2 tim8::natNT2 tim13::hphNT1* [pFL39-Tim9$_{V70S}$]	This paper	yNW-5100
YPH499 *tim9::ade2 tim8::natNT2 tim13::hphNT1* [pFL39-Tim9$_{L64S}$]	This paper	yNW-5099
YPH499 *tim10::ade2* [pFL39-Tim10$_{L26K}$]	This paper	yNW-5209
YPH499 *tim10::ade2* [pFL39-Tim10$_{L26Q}$]	This paper	yNW-5210
YPH499 *tim10::ade2* [pFL39-Tim10$_{V29K}$]	This paper	yNW-5106
YPH499 *tim10::ade2* [pFL39-Tim10$_{V29S}$]	This paper	yNW-5107
YPH499 *tim10::ade2* [pFL39-Tim10$_{M32K}$]	This paper	yNW-5108
YPH499 *tim10::ade2* [pFL39-Tim10$_{M32S}$]	This paper	yNW-5214
YPH499 *tim10::ade2* [pFL39-Tim10$_{F33Q}$]	This paper	yNW-5109
YPH499 *tim10::ade2* [pFL39-Tim10$_{V29KV76S}$]	This paper	yNW-5112
YPH499 *tim10::ade2* [pFL39-Tim10$_{V76S}$]	This paper	yNW-5122
YPH499 *tim10::ade2* [pFL39-Tim10$_{M80K}$]	This paper	yNW-5211
YPH499 *tim10::ade2* [pFL39-Tim10$_{F70S}$]	This paper	yNW-5120
YPH499 *tim10::ade2* [pFL39-Tim10$_{V76K}$]	This paper	yNW-5212
YPH499 *tim10::ade2* [pFL39-Tim10$_{F33QF70S}$]	This paper	yNW-5115
YPH499 *tim9::ade2* [pFL39-Tim9$_{M21K}$]	This paper	yNW-5126
YPH499 *tim9::ade2* [pFL39-Tim9$_{F24K}$]	This paper	yNW-5127
YPH499 *tim9::ade2* [pFL39-Tim9$_{M21KF24K}$]	This paper	yNW-5129
YPH499 *tim9::ade2* [pFL39-Tim9$_{L27K}$]	This paper	yNW-5213
YPH499 *tim9::ade2* [pFL39-Tim9$_{Y28Q}$]	This paper	yNW-5131
YPH499 *tim9::ade2* [pFL39-Tim9$_{L27SY28Q}$]	This paper	yNW-5132
YPH499 *tim9::ade2* [pFL39-Tim9$_{V70S}$]	This paper	yNW-5135
YPH499 *tim9::ade2* [pFL39-Tim9$_{L64S}$]	This paper	yNW-5134
Oligonucleotides		
See Table S3	This study/Eurofins	N/A
Recombinant DNA		
pFL39Tim9	Nils Wiedemann	pNW-2917
pFL39Tim10	Nils Wiedemann	pNW-2814
pFL39Tim9$_{M21K}$	This paper	pNW-2918
pFL39Tim9$_{M21S}$	This paper	pNW-2919
pFL39Tim9$_{F24K}$	This paper	pNW-2920
pFL39Tim9$_{M21KF24K}$	This paper	pNW-2921
pFL39Tim9$_{L27K}$	This paper	pNW-2922
pFL39Tim9$_{Y28Q}$	This paper	pNW-2923
pFL39Tim9$_{L27SY28Q}$	This paper	pNW-2924

(*Continued on next page*)

Continued

REAGENT or RESOURCE	SOURCE	IDENTIFIER
pFL39Tim9$_{V70S}$	This paper	pNW-2925
pFL39Tim9$_{V70K}$	This paper	pNW-2926
pFL39Tim9$_{F74K}$	This paper	pNW-2927
pFL39Tim9$_{L64S}$	This paper	pNW-2928
pFL39Tim10$_{V29K}$	This paper	pNW-2816
pFL39Tim10$_{V29S}$	This paper	pNW-2817
pFL39Tim10$_{M32K}$	This paper	pNW-2818
pFL39Tim10$_{M32S}$	This paper	pNW-2819
pFL39Tim10$_{F33Q}$	This paper	pNW-2820
pFL39Tim10$_{M32KF33Q}$	This paper	pNW-2821
pFL39Tim10$_{F33QF70S}$	This paper	pNW-2827
pFL39Tim10$_{V29KV76S}$	This paper	pNW-2825
pFL39Tim10$_{V76S}$	This paper	pNW-2831
pFL39Tim10$_{V76K}$	This paper	pNW-2929
pFL39Tim10$_{L26K}$	This paper	pNW-2836
pFL39Tim10$_{L26Q}$	This paper	pNW-2839
pFL39Tim10$_{F70S}$	This paper	pNW-2829
pFL39Tim10$_{M80K}$	This paper	pNW-2838
pFL39Tim10$_{L26KV29K}$	This paper	pNW-3097
pFL39Tim10$_{V29KF33Q}$	This paper	pNW-3098
pGEM-4Z-Tom40	Nils Wiedemann	pNW-1495
pGEM-4Z-Aac2	Nils Wiedemann	pNW-1039
pGEM-4Z-Aac2-DHFR	Nils Wiedemann	pNW-1253
pGEM-3Z-pSu9-DHFR	Nils Wiedemann	pNW-S02
pSP64-F1β	Nils Wiedemann	pNW-F01
pGem-4Z-Tim23	Nils Wiedemann	pNW-M36
pFA6a-hphNT1	Janke et al., 2004	http://www.euroscarf.deindex.php?name=News
pFA6a-natNT2	Janke et al., 2004	http://www.euroscarf.deindex.php?name=News
pETDuet-1 TIM9•10	This paper	pPS-TIM910_001
pET21a(+) Ggc1	Kurauskas et al., 2018	pPS-Ggc1_001
pET21a(+) Ggc1$_{C222S}$	GeneCust/Paul Schanda	pPS-Ggc1_E2
pET21a(+) Ggc1$_{C222S/C8Q}$	GeneCust/Paul Schanda	pPS-Ggc1_F6
pET21a(+) Aac3	GenScript/Paul Schanda	pPS-Aac3CtoAS_001
pET21a(+) Aac3(TM2)	GenScript/Paul Schanda	pPS-Aac3TM23CtoA_001
pETDuet-1 TIM9•10$_{V29K}$	GeneCust//Paul Schanda	pPS-TIM910_003
pETDuet-1 TIM9•10$_{M32K}$	GeneCust/Paul Schanda	pPS-TIM910_002
pETDuet-1 TIM9•10$_{F33Q}$	GeneCust/Paul Schanda	pPS-TIM910_004
pETDuet-1 TIM9•10$_{F33Q/F70S}$	GeneCust/Paul Schanda	pPS-TIM910_005
pETDuet-1 TIM9$_{V70K}$ •10	GeneCust/Paul Schanda	pPS-TIM910_010
pETDuet-1 TIM9$_{F74K}$ •10	GeneCust/Paul Schanda	pPS-TIM910_011
Software and Algorithms		
CCPNMR, version 2.4	Vranken et al., 2005	https://www.ccpn.ac.uk/v2-software/software/analysis
Bruker Topspin, version 3.5	Bruker Biospin	V 3.5
nmrPipe	Delaglio et al., 1995	http://nmrpipe.com/
ChemEx	Guillaume Bouvignies	https://github.com/gbouvignies/chemex

(*Continued on next page*)

Continued

REAGENT or RESOURCE	SOURCE	IDENTIFIER
MODELER, version 9.18	Webb and Sali, 2014	https://salilab.org/modeller/
ATSAS package (GNOM, Primus)	Svergun, 1992	https://www.embl-hamburg.de/biosaxs/download.html
BME	Bottaro et al., 2018	https://github.com/sbottaro/bme
GROMACS 5.1.4	Abraham et al., 2015	http://www.gromacs.org/
PLUMED 2.3	Tribello et al., 2014	http://www.plumed.org/
PULCHRA	Rotkiewicz and Skolnick, 2008	http://www.pirx.com/pulchra/
Crysol3	Franke et al.,2017	https://www.embl-hamburg.de/biosaxs/crysol.html
FoxS	Schneidman-Duhovny et al., 2013	https://modbase.compbio.ucsf.edu/foxs/
WAXSiS	Knight and Hub, 2015	http://waxsis.uni-goettingen.de/
Image Analyzer LAS-4000	Fujifilm	Image Reader V 1.12
Typhoon FLA7000	GE Healthcare	Image Reader V 2.1
Multi Gauge	Fujifilm	V 3.2
Geneious Pro	Biomatters	V 5.4.3
AB2 Luminescence Spectrometer	Thermo Electron	V 5.5
Pymol, version 1.8	Schrödinger	https://pymol.org/2/

CONTACT FOR REAGENT AND RESOURCE SHARING

Further information and requests for resources and reagents should be directed to and will be fulfilled by the Lead Contact, Paul Schanda (paul.schanda@ibs.fr).

EXPERIMENTAL MODEL AND SUBJECT DETAILS

For all *in vitro* experiments (in-vitro complex formation, NMR, SAXS, cross-linking), TIM9·10 chaperones and precursor proteins were produced in *Escherichia coli*, either in the strain BL21(DE3), for carrier precursor proteins, or in Shuffle T7, for TIM9·10 proteins, as described in detail in the respective sections.

S. cerevisiae strains in this study were YPH499 (genotypes listed in Key Resources Table). Cells were grown in YPG (3% glycerol) medium at permissive temperature (19-23°C). Alternatively for *in vivo* heat shock, yeast cells were grown in YPG medium for 6 h at 21°C and then shifted to 37°C for 14 h.

METHODS DETAILS

Protein constructs of TIM9·10 and carrier precursor proteins used for *in vitro* experiments

Plasmids for production of protein samples in *E. coli* containing the respective sequences of TIM9·10 and precursor proteins were purchased from GeneCust and Genscript. The cysteine residues of the wild-type precursor protein sequences, Ggc1, Aac3, Aac3(2TM), were replaced by either Ala or Ser residues. The respective protein sequences used in the *in vitro* experiments are listed below.

Tim9: MDALNSKEQQEFQKVVEQKQMKDFMRLYSNLVERCFTDCVNDFTTSKLTNKEQTCIMKCSEKFLKHSE RVGQRFQEQNAAL GQGLGR

Tim10: MGSSHHHHHHSQDPENLYFQ**G**SFLGFGGGQPQLSSQQKIQAAEAELDLVTDMFNKLVNNCYKKCINTSYSEGELNKNESS CLDRCVAKYFETNVQVGENMQKMGQSFNAAGKF, the cleavage of the N-terminal His-tag results in a sequence starting with the glycine highlighted in bold/underlined (the wild-type sequence starts with MSFL…).

Ggc1 (containing the mutation C222S): MPHTDKK**Q**SGLARLLGSASAGIMEIAVFHPVDTISKRLMSNHTKITSGQELNRVIFRDHFS EPLGKRLFTLFPGLGYAASYKVLQRVYKYGGQPFANEFLNKHYKKDFDNLFGEKTGKAMRSAAAGSLIGIGEIVLLPLDVLKIKRQTN PESFKGRGFIKILRDEGLFNLYRGWGWTAARNAPGSFALFGGNAFAKEYILGLKDYSQATWSQNFISSIVGA**S**SSLIVSAPLDVIKTR IQNRNFDNPESGLRIVKNTLKNEGVTAFFKGLTPKLLTTGPKLVFSFALAQSLIPRFDNLLSKLEHHHHHH

This sequence was used for all *in vitro* experiments with Ggc1, except for the paramagnetic labeling experiments for which, we also used the wild-type sequence, containing the native Cys at position 222, and a sequence containing C222S/Q8C mutation. These positions are highlighted above in bold face and underlined.

Aac3: MASMTGGQQMGRGSHHHHHHHHHHLVPMSSDAKQQETNFAINFLMGGVSAAIAKTAASPIERVKILIQNQDEMIKQGTLDK
KYSGIVDAFKRTAKQEGLISFWRGNTANVIRYFPTQALNFAFKDKIKLMFGFKKEEGYGKWFAGNLASGGAAGALSLLFVYSLDFART
RLAADAKSSKKGGARQFNGLTDVYKKTLKSDGIAGLYRGFMPSVVGIVVYRGLYFGMFDSLKPLVLTGSLDGSFLASFLLGWVVTTG
ASTASYPLDTVRRRMMMTSGQAVKYNGAIDALKKIVASEGVGSLFKGSGANILRSVAGAGVISMYDQLQMILFGKKFK
Aac3(2TM), comprising transmembrane helices 2 and 3 (residues 50-180): HHHHHHGTLDKKYSGIVDAFKRTAKQEGLISFWRGN
TANVIRYFPTQALNFAFKDKIKLMFGFKKEEGYGKWFAGNLASGGAAGALSLLFVYSLDFARTRLAADAKSSKKGGARQFNGLTDVY
KKTLKSDGIAGLYR

Buffers mentioned in the descriptions below

Buffer A: 50 mM Tris buffer (tris(hydroxymethyl)aminomethane), pH 7.4, 150 mM NaCl
Buffer B: Buffer A supplemented with 20 mM imidazole and 0.5 M NaCl.
Buffer C: Buffer A supplemented with 0.5 M imidazole.
NMR buffer: 20 mM MES buffer (2-(N-morpholino)ethanesulfonic acid), pH 6.5, 50 mM NaCl

Cloning, expression and purification of TIM9·10

Saccharomyces cerevisiae TIM9 was cloned via NdeI/XhoI into the MCS2 of pETDuet-1, subsequently *Saccharomyces cerevisiae TIM10* containing a N-terminal TEV (Tobacco etch virus) cleavage site was cloned via BamHI/HindIII into the MCS1.

Tim9 and His-tagged Tim10 were co-expressed in SHuffle T7 *E. coli* cells (New England Biolabs). After induction at OD_{600} 0.8 with 0.5mM IPTG (Isopropyl-β-D-1-thiogalactopyranoside), cells were incubated at 20°C overnight and harvested by centrifugation.

The cell pellet was resuspended in 25 mL buffer A per liter of cell culture and sonicated for 5 min (2 s on / 8 s off at 50% amplitude). After a heat shock for 15 min at 80°C the soluble fraction was separated from the insoluble fraction by centrifugation at 40000 x g for 30 min. The supernatant was loaded on a Ni-NTA affinity column pre-equilibrated with buffer A, then washed with 10 column volumes (CV) buffer B. Hexameric TIM9·10 complex was eluted with buffer C. The His-tag was cleaved overnight in buffer A supplemented with 0.5 mM DTT (1,4-Dithiothreitol) and 0.5 mM EDTA (ethylene diaminetetraacetic acid) by adding 1 mg TEV protease to 50 mg protein, cleaved TIM9·10 was separated from uncleaved TIM9·10 on a Ni-NTA column using the above described protocol. The load and wash fractions were then further purified on a HiLoad 16/60 Superdex S200 pg, where TIM9·10 eluted as a single peak. For samples used in NMR experiments, gel filtration was performed with NMR buffer.

To purify the individual subunits of the TIM9·10 complex, an additional washing step was included into the Ni-NTA purification protocol: after washing with buffer B, the column was washed with 10 CV of buffer B supplemented with 3 M guanidine-HCl to dissociate the TIM9·10 complex. While His-tagged Tim10 was still bound to the Ni-NTA column, Tim9 was found only in the wash fraction. His-Tagged Tim10 was eluted with buffer C supplemented with 3 M guanidine-HCl and refolded by flash dilution into buffer A, the His-tag was cleaved as described above. The wash fraction including Tim9 was dialyzed into buffer A and both (Tim9 and Tim10) subjected to gel filtration on a HiLoad 16/600 75 PG. Tim9 was found to elute as a dimer, Tim10 mainly as a monomer.

Expression and purification of TIM9·10 substrates Ggc1, Ggc1-C222S, Ggc1-C222S/C8Q, Aac3 and Aac3(2TM)

Saccharomyces cerevisiae GGC1 constructs were purchased from GeneCust in pET21b, Aac3 constructs in pET21a plasmids. Ggc1 constructs were designed with a C-terminal 6xHis-tag, Aac3(2TM) with a N-terminal 6xHis-Tag and Aac3 with a N-terminal 9xHis-Tag as shown above.

All TIM9·10 substrates were expressed in BL21(DE3) *E. coli* cells as inclusion bodies. Cells were grown at 37°C until an OD_{600} of 0.7 was reached and induced with 1 mM IPTG for 3 hr. The cell pellet was resuspended in buffer A, sonicated and centrifuged at 39121 x g for 30 min. The inclusion body pellet was resuspended in buffer A supplemented with 6 M guanidine-HCl (for scGgc1 wild-type 2 mM DTT were added to each purification step) and incubated at 4°C for 16 hr. The solubilized inclusion bodies were separated from the insoluble fraction by centrifugation and loaded on a Ni-NTA resin. Proteins were purified as described for TIM9·10 with addition of 3 M guanidine-HCl to all buffers.

Isotope labeling

For NMR experiments TIM9·10 was expressed in D_2O M9 minimal medium and either labeled with 1 g/L [^{15}N] NH_4Cl and 2 g/L D-[^{2}H,^{13}C] glucose or specifically labeled on alanine, leucine and valine side chains using the SLAM-A^{β} and DLAM-^{LVproS} kit from NMR-Bio (http://www.nmr-bio.com) according to the manufacturer's instructions. Accordingly, Ggc1-C222S was labeled on alanine and isoleucine side chains using the DLAM-$A^{\beta}/I^{\delta1}$ kit from NMR-Bio.

Site-specific spin-labeling of scGGC1

Ggc1 containing one Cys residue (at position 8 or 222, see sequences above) was incubated for 1 hr at room temperature in 6 M guanidine-HCl with 10 mM DTT. Subsequently DTT was removed on an illustra NAP25 column and the protein was incubated

with a three-fold molar excess of MTSL (1-oxyl-2,2,5,5-tetramethyl-Δ3-pyrroline-3-methyl)-methanethiosulfonate) dissolved in DMSO (dimethyl sulfoxide) for 16 hr at 4°C in the dark. Free MTSL was removed on an illustra NAP25 column. Efficiency of the spin labeling reaction was confirmed by continuous-wave electron paramagnetic resonance spectroscopy.

Production of chaperone-precursor protein complexes

Purified inner-membrane protein (Aac3, Ggc1, Aac3(2TM)) in 6 M guanidine-HCl was bound to Ni-NTA resin and washed with 5 CV of 1 M guanidine-HCl. Subsequently, a twofold excess of TIM9·10 was added to the column in 1/5 of the CV. The flow-through containing TIM9·10 was collected, diluted 1:1 with buffer A and reloaded on the column. This step was repeated until 10 CV were reached and the guanidine-HCl concentration was below 0.05 M. The column was washed with another 5 CV of buffer A, the TIM9·10-substrate complex eluted with 5 CV of buffer C and dialyzed into buffer A or NMR buffer. We note that this approach was unsuccessful for producing complexes with outer-membrane precursor proteins, presumably because of the requirement for pre-formed β-hairpin structures, as demonstrated by the different binding behavior of linear and cyclic $VDAC_{257-279}$ peptides.

Cell-free expression of Ggc1 in the absence or presence of TIM9·10

Ggc1 with a C-terminal HisTag in pIVEX 2.3d was expressed under cell-free conditions in batch mode for 2 h at 30°C, as described in Table S3 and in the caption of Figure S1A. In the presence of the TIM9·10 complex, aggregation of the nascent *in vitro* translated Ggc1 is prevented by formation of a soluble chaperone/precursor protein complex (Figure S1A).

Analytical ultracentrifugation

Sedimentation velocity experiments were performed on the Biophysical Platform AUC-PAOL at IBS Grenoble, on an analytical ultracentrifuge XLI, with a rotor Anti-50 (Beckman Coulter, Palo Alto, USA) and double-sector cells of 12 mm and 1.5 mm optical path length equipped with Sapphire windows (Nanolytics, Potsdam, Germany).

Samples were measured in NMR buffer at 10°C at three different concentrations from 0.2 to 0.002 mM, and interference and absorption at 277 nm wavelength were recorded. The data were processed by Redate software v 0.2.1. The analysis was done with the SEDFIT software, version 14.7 g and Gussi 1.1.0a6.

Circular dichroism spectroscopy

Far ultraviolet (FUV) CD spectra were recorded in a 1 mm cell at 0.1 mg/mL protein concentration at 35°C in buffer A on a Jasco J-810 spectropolarimeter continuously purged with nitrogen.

NMR spectroscopy

All NMR experiments were performed on Bruker Avance III spectrometers equipped with cryogenically cooled TCI probeheads, operating at magnetic field strengths corresponding to ^{1}H Larmor frequencies of 950, 850, 700 and 600 MHz, respectively. The sample temperature was set to 308 K, unless stated otherwise.

Sequence-specific resonance assignments of TIM9·10

Assignment experiments were performed on TIM9·10 complexes with individually labeled subunits. To this end [^{2}H]-labeled His-tagged Tim10 was mixed with a 1.2-fold excess of [^{2}H,^{13}C,^{15}N]-labeled Tim9 and purified on a Ni-NTA column as described above. Unbound Tim9 was found in the wash fraction, while hexameric TIM[^{2}H,^{13}C,^{15}N]9·[^{2}H]10 was eluted. The His-tag was cleaved as described above and the complex subjected to gel filtration on a HiLoad 16/600 Superdex S200 PG in NMR buffer. To obtain TIM [^{2}H]9[^{2}H,^{13}C,^{15}N]10, the protocol was repeated with [^{2}H,^{13}C,^{15}N] His-tagged Tim10 and [^{2}H] Tim9.

The following experiments were recorded: 2D ^{15}N-^{1}H-BEST-TROSY HSQC, 3D BEST-TROSY HNCO, 3D BEST-TROSY HNcaCO, 3D BEST-TROSY HNCA, 3D BEST-TROSY HNcoCA, 3D BEST-TROSYHNcocaCB and 3D BEST-TROSY HNcaCB (Favier and Brutscher, 2011).

Methyl groups Ala^{β}, Leu^{proS} and Val^{proS} were assigned using 3D ^{1}H-^{1}H-NOESY-^{13}C-HSQC and 4D ^{15}N-HSQC-NOESY-^{13}C-HSQC with 300ms mixing time. The assignment of the Ala^{β} ^{13}C resonance was independently confirmed from the HNCACB experiment.

Data were processed in NMRPipe (Delaglio et al., 1995) and analyzed with CCPNMR (Vranken et al., 2005). Resonance assignments of backbone and ALV methyl sites were deposited in the BioMagResBank under accession number BMRB: 27052.

Diffusion ordered spectroscopy

Diffusion constants were derived from methyl-directed one-dimensional ^{13}C filtered DOSY experiments (Didenko et al., 2011) performed at 600 MHz ^{1}H Larmor frequency. All samples were measured at a concentration of 70 μM at 308 K in NMR buffer with 10% (v/v) D_2O. Three samples were measured: $^{13}CH_3$-ALV TIM9·10, $^{13}CH_3$-ALV TIM9·10 in complex with unlabeled Ggc1 and unlabeled TIM9·10 in complex with $^{13}CH_3$-Al Ggc1. Peak integrals were obtained from 1D integration over the methyl band.

Methyl order parameter measurements from relaxation-violated coherence transfer NMR

A triple-quantum based relaxation-violated coherence transfer experiment was performed to measure the fast methyl dynamics in TIM9·10 and in TIM9·10/Ggc1, i.e., the product of site-specific methyl-axis order parameter, S^2, and the overall-tumbling correlation time constant, τ_c. TIM9·10, labeled at $^{13}CH_3$-ALV groups in an otherwise perdeuterated environment was either measured in the apo form or with bound Ggc1 (unlabeled), in D_2O 20 mM MES-d_{13} 50 mM NaCl pD 6.1 (D_2O NMR buffer). The experiments were recorded at a ^{1}H Larmor frequency of 950 MHz, according to reference (Sun et al., 2011). 12 different values of the 3Q relaxation delay (delay

T in reference (Sun et al., 2011)) were acquired, from 1.1 to 35 ms. The ratio of peak integrals in the relaxation-violated coherence transfer (I_a) and the reference experiment (I_b) as a function of the relaxation delay T were fitted as described in the section 'Quantification And Statistical Analysis'.

CPMG experiments

^{1}H-^{13}C multiple-quantum relaxation dispersion experiments (Korzhnev et al., 2004) were recorded to probe millisecond motion of methyl groups in TIM9·10, TIM9·10/Ggc1, TIM9·10/Aac3 and Ala^{β}/$Ile^{\delta1}$ methyls in Ggc1 bound to TIM9·10. The samples were either $^{13}CH_3$-ALV TIM9·10, or $^{13}CH_3$-ALV-labeled TIM9·10 in complex with unlabeled Ggc1, or $^{13}CH_3$-Ala^{β}/$Ile^{\delta1}$-labeled Ggc1 bound to unlabeled TIM9·10. The CPMG relaxation period was set to 40 ms (TIM9·10 and TIM9·10/Ggc1) or 60 ms (TIM9·10/Aac3). The CPMG frequency applied for 40 ms was 0, 50, 100, 150, 200, 250, 300, 350, 400, 500, 600, 700, 800, 900 and 1000 Hz and for 60 ms 66, 133, 200, 267, 333, 400, 466, 533, 600, 733, 867, 1000 Hz. Additionally, a reference experiment with no CPMG relaxation period was performed and the effective relaxation rate constant R_{2eff} was obtained from the peak volumes in this reference experiment, I_0, and the pek volumes in the CPMG experiment, $I(\nu_{CPMG})$, as $R_{2eff} = -1/T \cdot \ln(I(\nu_{CPMG}) / I_0)$. Experiments were performed at different static magnetic field strengths (600, 700, 850, 950 MHz), as stated in the caption of Figure 6D.

^{1}H intermolecular cross-relaxation experiments for measuring transferred NOEs

To detect the contact surface of Ggc1 with TIM9·10, we probed the effect of ^{1}H spin saturation transfer, i.e., a NOE-type transfer, from unlabeled Ggc1 to a deuterated $^{13}CH_3$-ALV-labeled TIM9·10. The principle of this measurement is identical to previously proposed HET-SOFAST experiments (Schanda et al., 2006), except that we apply this concept here to methyls, rather than backbone amides. The effect of saturation transfer, i.e., cross-relaxation from the protons of Ggc1 to TIM9·10, is monitored by measuring the intensity of TIM9·10 methyl peaks in two experiments. The first dataset (I_{ref}) is a standard ^{1}H-^{13}C SOFAST experiment, using a recycle delay of 0.2 s. In a second experiment (I_{sat}), an inversion pulse is applied at the beginning of the recycle delay, which inverts protons of Ggc1. If a given TIM9·10 methyl site is in close spatial proximity, the effective ^{1}H longitudinal relaxation during the recycle delay will be slowed down in this latter experiment, because of the intermolecular cross-relaxation. The inversion pulse (ISNOB2 [Kupce et al., 1995]) was applied at 4 ppm with a band width of 2 ppm, i.e., in a spectral region that is devoid of TIM9·10 resonances, due to the > 98% deuteration. The differential longitudinal relaxation of methyl ^{1}H spins on TIM9·10 that arises from the intermolecular cross-relaxation can be monitored by the ratio of the intensities in the two experiments, I_{sat}/I_{ref}. To ensure that artifacts due to residual (< 2%) protonation of TIM9·10 do not introduce bias, we recorded these experiments not only on $^{13}CH_3$-ALV-TIM9·10 bound to unlabeled Ggc1, but also on $^{13}CH_3$-ALV-TIM9·10 in the absence of Ggc1. In this latter experiment no inter-molecular cross-relaxation can occur. The values reported in Figure 1C have been corrected by the values obtained in this reference experiment.

In all cases, the samples were in D_2O buffer, and the experiments were recorded at a ^{1}H Larmor frequency of 950 MHz.

PRE experiments

A complex between $^{13}CH^{3}$-ALV-TIM9·10 and MTSL-labeled Ggc1 containing a single Cys residue either at position 8 (Q8C) or 222 (wild-type) was prepared as described above. Methyl ^{1}H R_1 relaxation was measured for this TIM9·10/$Ggc1_{MTSL}$ complex, and a sample in which the MTSL spin label was reduced by addition of 5 mM sodium ascorbate via a saturation-recovery experiment. Hereby, the recovery delay following the saturation element was incremented from zero to 3 s, and the site-specific buildup rate constants were fitted by a mono-exponential function. The effect of the paramagnetically tagged Ggc1 was monitored via the difference between R_1 relaxation rate constants between the paramagnetic and the ascorbate-reduced sample.

NMR-based measurement of precursor protein transfer kinetics between chaperones

To probe at which rate precursor protein is transferred between TIM9·10 chaperones, we have prepared a complex of unlabeled TIM9·10 with ^{2}H,^{15}N-labeled Aac3(2TM), and concentrated to 300 μM in NMR buffer. The ^{15}N-labeling of the precursor protein allows verifying the state of the precursor protein. 60 μL of this solution were mixed with 100 μL of ^{2}H, ALV-methyl labeled TIM9·10 at a concentration of 160 μM, resulting in concentrations of 100 μM ALV-TIM9·10, 112 μM Aac3(2TM) and 112 μM unlabeled TIM9·10. The dead time between mixing of the solutions and acquisition of the first NMR spectrum was 5 min.

The intensity of the methyl resonances was followed through a series of ^{1}H,^{13}C SOFAST-HMQC experiments. The number of scans was varied from 2 (to capture the initial phase of the decay; duration of one 2D experiment: 3 min 50 s) to 64 for the last data points for enhanced signal-to-noise ratio (duration of one 2D experiment: 2 hr). The peak intensities from well-resolved cross-peaks of residues in the binding cleft or at the top of the TIM9·10 structure, outside the binding cleft, were determined in CCPNMR, and exported for fitting with in-house written Python scripts. Monoexponential fits of the intensity decays of individual peaks in the binding cleft revealed similar kinetic rate constants, as expected for the global process in which apo TIM is converted to precursor-protein-loaded TIM. To increase signal-to-noise ratio, peak intensities of residues in the binding cleft and at the top of the chaperone were added up as indicated in Figure 6H.

The fact that residues outside the binding cleft show near-constant intensity allows us to exclude that the sensitivity drop observed for binding cleft residues is due to, e.g., precipitation of the protein.

The expected intensity plateau level after equilibration of the reaction, relative to the initial intensity is, thus, given by the ratio of intensities observed in (equilibrium) holo and apo samples (I_{holo}/I_{apo}; Figure S1G) and the respective concentrations of labeled and unlabeled TIM in the mixed sample ([TIM_{lab}], [TIM_{unlab}]), as $I_{plateau} = ((I_{holo}/I_{apo}*[TIM_{lab}]) + (1*[TIM_{unlab}])) / ([TIM_{lab}]+ [TIMun_{lab}])$. For example, for a residue with a I_{holo}/I_{apo} ratio of 0.5 and the concentrations used in the mixed sample according to our experiment (see above), the plateau level is expected at 0.76.

The experiment was repeated twice with independent samples, resulting in similar exchange kinetic rate constants (not shown).

VDAC peptide titration

VDAC peptides were chemically synthesized as described elsewhere (Jores et al., 2016), lyophilized, and dissolved in DMSO. The DMSO concentration was reduced by stepwise addition of NMR buffer (1:1 in each step). At a DMSO concentration of 10% (v/v), TIM9·10 in NMR buffer was added instead of pure NMR buffer to yield a final DMSO concentration of 6% and a TIM9·10 concentration of 0.15 mM. NMR intensities and peak positions of the LV-$^{13}CH_3$ groups and amide backbone sites of TIM9·10 were obtained from 2D ^{1}H-^{13}C HMQC and ^{1}H-^{15}N HSQC experiments, using samples containing VDAC peptides at molar ratios of 1:0 to 1:4, as shown in Figures 2B and 2C and S2. In all cases, the DMSO concentration was kept to 6% to ensure comparability.

Cross-linking of VDAC peptides to TIM9·10

Synthesis of the Bpa-containing linear and cyclic β-hairpin peptides was described before (Jores et al., 2016). *In vitro* photo-cross-linking was performed by mixing the purified TIM9·10 complex (5 μM) with Bpa-containing β-hairpin peptides at concentrations of 25 μM or 50 μM, as indicated in the Figure 2A, in crosslinking buffer (20 mM HEPES, 100 mM NaCl, 1.5 mM $MgCl_2$, pH 7.25). The mixture was incubated for 10 min on ice before UV-irradiation for 30 min at 4°C using a Blak-Ray B-100 AP UV lamp at a distance of 10 cm from the samples. After UV-illumination, the samples were mixed with 4x Laemmli buffer, incubated at 95°C for 5 min and analyzed by SDS-PAGE and silver staining.

Small-angle X-ray scattering data collection and analysis

SAXS data were collected at ESRF BM29 beam line (Pernot et al., 2013) with a Pilatus 1M detector (Dectris) at the distance of 2.872 m from the 1.8 mm diameter flow-through capillary. Data on TIM9·10 were collected in a batch mode. The scattering of pure water was used to calibrate the intensity to absolute units. The X-ray energy was 12.5 keV and the accessible q-range 0.032 nm^{-1} to 4.9 nm^{-1}. The incoming flux at the sample position was in the order of 10^{12} photons/s in 700x700 μm^2. All images were automatically azimuthally averaged with pyFAI (Ashiotis et al., 2015). SAXS data of pure TIM9·10 was collected at 1, 2.5 and 5 mg/mL using the BioSAXS sample changer (Round et al., 2015). Ten frames of 1 s were collected for each concentration. Exposures with radiation damage were discarded, the remaining frames averaged and the background was subtracted by an online processing pipeline (Brennich et al., 2016). Data from the three concentrations were merged following standard procedures to create an idealized scattering curve of TIM9·10, using Primus from the ATSAS package (Petoukhov et al., 2012). The pair distribution function p(r) was calculated using GNOM (Svergun, 1992).

Online purification of the TIM9·10/Ggc1 complex using a NiNTA column was performed with a high pressure liquid chromatography (HPLC) system (Shimadzu, France), as described in reference (Brennich et al., 2017). The HPLC system was directly coupled to the flow-through capillary of SAXS exposure unit. The buffer used in this experiment was Buffer A. The flow rate for all online experiments was 0.2 mL/min. Data collection was performed continuously throughout the chromatography run at a frame rate of 1 Hz. The stoichiometry of the individual peaks in the chromatogram was determined from molecular mass estimates based on the correlated and Porod volumes (Petoukhov et al., 2012) and by calculating the ratios of maximum forward scattering and maximum absorbance at 280 nm for each peak and comparing to the theoretical values of different stoichiometries. For creating background corrected scattering curves for the TIM9·10:Ggc1 2:1 complex peak, measurements of buffer with the lowest (200 mM) and the highest (300 mM) possible imidazole concentration, as well as interpolated curves between these two extremes, were subtracted individually from each frame. The resulting curves were independent of protein concentration, as shown with procedures outlined by Hynson et al. (2015). Subtraction of the highest imidazole concentration provided a stable signal throughout the center of the peak. 50 frames from the middle of the peak were averaged to create a single SAXS curve for the TIM9·10:Ggc1 2:1 complex. For all subsequent analyses, the robustness of the main findings (general shape and dimensions) was confirmed by analogous treatment of curve resulting from the subtraction of the lowest possible imidazole concentration. The pair distribution function p(r) was calculated using GNOM. SAXS data along with their MD-derived models (described below) are shown in Figure S6 and the experimental and fit parameters are reported in Table S4. SAXS data reported in this study have been deposited in the SASBDB data bank (https://www.sasbdb.org) with accession numbers SASDEF2 (TIM9·10) and SASDEG2 (TIM9·10/Ggc1).

Molecular dynamics simulations

(a) All-atom MD simulation of apo-TIM9·10

We used the crystal structure (PDB ID 3DXR [Webb et al., 2006]) as the initial model of the TIM9·10 hexamer. Missing residues were added using MODELLER9.18 (Webb and Sali, 2014). The protein was solvated in a cubic box of TIP3P water molecules with sides of 10.6 nm and periodic boundary conditions. The Amber ff99SB*-ILDN force field (Lindorff-Larsen et al., 2010) was used for the simulations. The temperature and pressure were kept constant at 298 K using the v-rescale thermostat with a 1 ps coupling constant and at 1.0 bar using the Parrinello-Rahman barostat with a 2 ps time coupling constant, respectively. We employed the virtual sites for hydrogen atoms with a single LINCS iteration (expansion order 6) and constrained the bonds involving hydrogen atoms using the LINCS algorithm, allowing simulations to be performed with an integration time step of 5 fs. The long-range electrostatic interactions were calculated by the means of the particle mesh Ewald decomposition algorithm with a 0.16 nm mesh spacing. A one-microsecond MD simulation was performed to collect the conformations of the apo TIM9·10 hexamer for further SAXS guided ensemble refinement using a maximum entropy method as described in the following section. The all-atom simulation revealed the upper part of the

α helices of the TIM9·10 hexamer are rigid, and are increasingly flexible toward their extremities, i.e., toward the N- and C-termini of the subunits (Figure S5B).

(b) Coarse-grained MD simulations of the TIM9·10/Ggc1 complex

To enhance the sampling of the TIM9·10/Ggc1 complex, we employed a simplified model in which each residue is coarse-grained into two beads (except glycines) to represent the backbone and side chain, respectively. One bead (C_A) is located at the position of the C_α atom. The other bead (C_B) is located at the center of mass of the side chain atoms. The basic idea was to combine a structure-based model for the folded chaperone with a more transferable model, which also includes non-native hydrophobic and electrostatic forces, to describe the interactions between the chaperone and carrier protein, and within the carrier protein. More specifically, the energy function of the coarse-grained model can be expressed by:

$$V_{CG} = V_{SB} + V_{charge} + V_{hydrophobic} + V_{restraints},$$

where V_{SB} is the structure-based potential to describe the local dynamics of the TIM9·10 hexamers around its crystal structure (PDB ID 3DXR). The V_{SB} term can be divided into local (bonded) and non-local terms. The non-local part of V_{SB} can be further partitioned into two components consisting of an attractive term, which is a function of the native contact map to stabilize the secondary and tertiary structures, and a repulsive term to provide the excluded volume. A detailed description of V_{SB} can be found in ref. (Clementi et al., 2000; Wang et al., 2013). V_{charge} and $V_{hydrophobic}$ are the electrostatic and hydrophobic potential, respectively, to describe the non-native interactions between TIM hexamers and Ggc1. V_{charge} is represented by the Debye-Hückel model (Wang et al., 2013) which is a linearization of the Poisson-Boltzmann equation. The charge states of C_B beads were assigned according to their possible electrostatic properties at neutral pH (1.0 for Lys and Arg, −1.0 for Asp and Glu and 0.5 for His in our model). $V_{hydrophobic}$ is expressed by:

$$V_{hydrophobic} = \varepsilon_{HP} \sum_i \sum_j - K_{ij} e^{-0.5\left(R_{ij} - D_{HP}\right)^2}$$

where R_{ij} is the distance between C_B beads *i* and *j*, D_{HP} is the optimal distance to form interfacial hydrophobic interactions, and K_{ij} is the strength of the hydrophobic interaction between C_B beads i and j. The K_{ij} matrix (in units of kJ mol^{-1}) is transformed from the original Miyazawa-Jernigan matrix (Miyazawa and Jernigan, 1996). We set ε_{HP} = 0.92 and D_{HP} = 5.0 Å which have been calibrated by Wang et al. (2014) for eight di-ubiquitin systems.

We supplemented the model outlined above with information from NMR on the site where TIM binds to Ggc1. In particular, we constructed a non-specific potential term that encourages Ggc1 to form contacts with those residues on TIM that were found by NMR to interact with the carrier proteins. This was achieved by adding an energy term, $V_{restraints}$, which is a half-harmonic potential of the form of $V_{restraints} = k(Q - Q_{ref})^2$ when the value of Q is lower than a certain limit Q_{ref}, and zero when $Q > Q_{ref}$. Here Q is the coordination number to define the sidechain contacts between Ggc1 and the binding site of TIM9·10 (M21, F24, L27, Y28 and F74 for TIM9, and L26, L28, V29, M32, F33, M80 for TIM10). We used Q_{ref} = 28 and k = 20kJ mol^{-1}.

MD simulations were performed with GROMACS 5.1.4 (Abraham et al., 2015) at temperature T = 60 (in reduced units) combined with the PLUMED 2.3 plugin (Tribello et al., 2014). A time step of 0.5 fs was used and the simulation was coupled to a temperature bath via Langevin dynamics with a coupling time of 1.0. We performed sixteen MD simulations of the TIM/Ggc1 complex starting from eight different initial conformations (Figure S6E) which were modeled manually using PyMol and energy minimized by the steepest descent algorithm. 14 million MD time steps (7 ns) were performed for each of the 16 trajectories, resulting in a total of 112 ns. Note that the actual timescale sampled is orders of magnitude longer, due to the enhanced sampling and simplified energy function employed.

Workflow of the ensemble refinement using SAXS data

1) First, we collected the conformational pools of the apo TIM hexamer and the TIM9·10/ Ggc1 complex as large as possible by MD simulations with all-atom or coarse-grained models (see above). For the TIM9·10/Ggc1 complex, the atomistic structures were reconstructed from the C_α coordinates of the coarse-grained trajectories using PULCHRA (Rotkiewicz and Skolnick, 2008).
2) We back-calculated the SAXS curve of each frame using Crysol3 (Franke et al., 2017). For a few frames we also compared with FoxS (Schneidman-Duhovny et al., 2013) (like Crysol uses a fast but implicit description of the hydration layer) and WAXSiS (Knight and Hub, 2015) (slower but with an explicit model for both the hydration layer and the excluded solvent), and found that the SAXS calculation by Crysol3 matched rather closely those from WAXSiS (data not shown), but with the computational cost as low as FoxS. Accordingly, we used Crysol3 in this work to balance the accuracy and computational cost.
3) We employed the maximum entropy approach (Bottaro et al., 2017; Hummer and Köfinger, 2015) to refine the simulated ensembles so as to match experimental SAXS data. Briefly, the ensemble refinement method attempts to adjust the prior conformational weights of frame *j* $(\omega_j^0 \rightarrow \omega_j)$ so as to minimize the target 'free-energy-like' function

$$F(\omega_j) = \frac{M}{2}\chi^2 - \theta S_{rel}$$

where

$$\chi^2 = \frac{1}{M}\sum_i^M \frac{\left(\sum_j^N w_j I_i^{calc}(x_j) - I_i^{exp}\right)^2}{\sigma_i^2}$$

measures the deviation from the experimental averages, M is the number of data points in the scattering profile, $I_i^{calc}(x_j)$ is the intensity back-calculated from the atomic coordinates of frame j (x_j), N is the number of conformers used for back-calculating the average scattering data, and $S_{rel} = -\sum_j^N \omega_j \ln(\omega_j/\omega_j^0)$ is the Kullback-Leibler divergence (relative entropy) which measures the deviation from the prior uniform distribution $\omega_j^0 = 1/N$. In this work, we sampled 1,000 conformers (N = 1,000, with one snapshot per ns) for the apo TIM and ~70,000 conformers (N = 70,000) for the holo TIM9·10/Ggc1 complex. In the Maximum Entropy/Bayesian formalism, θ is a free 'temperature-like' parameter to control the relative contribution of χ^2 and S_{rel} terms. For large θ, the ensemble refinement algorithm leads to small perturbations of the initial weights (small Kullback-Leibler divergence), whereas for small θ, it is possible to change the weights substantially to obtain the best possible agreement with the experimental scattering data, but possibly have the risk of over-fitting. One may find an appropriate choice of θ by inspecting the relative entropy S_{rel} against the χ^2 obtained in reweighting for different values of θ (Figures S6F–S6I): as θ is lowered one gradually obtains an improved fit, but at the smallest values of θ one only obtains marginal improvements in fit quality at the cost of a substantial loss of entropy (i.e., a large deviation from the molecular dynamics ensemble). The software to perform the ensemble refinement is available from https://github.com/sbottaro/bme, and we used the back-calculated scattering data for apo TIM (θ = 729) and the TIM9·10/Ggc1 complex (θ = 1369) (Figures S6F–S6I). The comparison of the final results with experimental scattering data is shown in Figures S6A–S6D.

4) Lastly, to provide a simpler way for visualizing the ensembles, we reconstructed a sub-ensemble by randomly picking 1,000 frames with individual probabilities proportional to their reweighting weights in the conformational pool. These conformations were then clustered (Daura et al., 1999) with an RMSD cut-off of 0.8 nm after aligning the structure by the position of two TIM hexamers. We repeated the reconstruction process three times, and all resulted in similar sub-ensembles. The top twelve clusters occupy ~80% of the conformational space of the sub-ensemble, as illustrated in Figure 7E.

Yeast handling and growth conditions

Since *TIM9* and *TIM10* are essential genes, *tim9* and *tim10* mutants were introduced into *Saccharomyces cerevisiae* by plasmid shuffling, to exchange *TIM9* or *TIM10* wild-type with the mutated version of *tim9* or *tim10* in a YPH499 background. Shuffle strains for Tim9 and Tim10 were used, harboring the genomic deletion of *TIM9* or *TIM10* complemented by the *URA3* selectable plasmid, YEp352, containing the *TIM9* or *TIM10* wild-type gene. To study the defects in *tim9* and *tim10* mutants in the absence of the homologous complex Tim8-Tim13, shuffle strains lacking *TIM8* and *TIM13* in addition to the genomic deletion of *TIM9* or *TIM10* were transformed (*tim9*Δ *tim8tim13*ΔΔ + YEp352-Tim9 or *tim10*Δ *tim8tim13*ΔΔ + YEp352-Tim10). The genomic deletion of *TIM8* and *TIM13* was introduced by homologous recombination according to the protocol of Janke et al. (2004). According to the protocol, PCR cassettes were amplified from genomic DNA with S1 and S2 primers, containing the antibiotic resistance for nourseothricin (*natNT2*) (Tim8) or hygromycin (*hphNT1*) (Tim13) flanked by homologous regions up- and downstream of the target gene. The chromosomal integration of the amplified cassettes led finally to the deletion of *TIM8* and *TIM13* (*tim9*Δ *tim8tim13*ΔΔ + YEp352-Tim9 or *tim10*Δ *tim8tim13*ΔΔ + YEp352-Tim10), which was verified by colony PCR.

Centromeric pFL39 plasmids with the yeast selectable marker *TRP1*, encoding the *tim9* or *tim10* mutants under the control of the endogenous promoter and terminator (pFL39-*tim9* or pFL39-*tim10*), were transformed into the shuffle strains by the lithium acetate method of Gietz and Woods. After *TRP1* selection (0.67% [w/v] yeast nitrogen base without amino acids (Becton Dickinson), 3% [w/v] agar (Becton Dickinson), 0.077% [w/v] SC amino acids without tryptophan (-TRP) (MP Biomedicals), 2% [v/v] glucose (Roth)), yeast clones were selected on 5FOA (5-Fluoroorotic acid) containing agar medium (0.065% [w/v] yeast nitrogen base without amino acids (Becton Dickinson), 3% [w/v] agar (Becton Dickinson), 0.077% [w/v] SC amino acids without uracil (-URA) (MP Biomedicals), 2% [w/v] glucose (Roth), 0.005% [w/v] uracil (Fluka Analytical), 0.065% [w/v] 5FOA (Melford)), selecting for clones, which lost the *URA3* plasmid YEp352 encoding wild-type *TIM9* or *TIM10*. Finally, clones were streaked on YPG medium (1% [w/v] yeast extract (Becton Dickinson), 2% [w/v] bacto peptone (Becton Dickinson), 3% [w/v] glycerol (Sigma), 3% [w/v] agar (Becton Dickinson)) to exclude the loss of mitochondrial DNA. During all transformation steps, cells were incubated at 23°C to minimize temperature sensitive growth phenotypes. Mutations, which did not give rise to at least two viable colonies after three rounds of plasmid shuffling were considered lethal.

To study the growth phenotype of the mutants, 4 mL YPG medium were inoculated with yeast and grown over night at 23°C and shaking at 130 rpm. Yeast cells corresponding to an OD_{600} of 1 were centrifuged for 5 min at 1,500 x g (4,000 rpm, Eppendorf 5424). The cell pellet was taken up in 1 mL sterile dH_2O and 3 µl of a serial yeast dilution (1:10, 1:100, 1:1,000, 1:10,000) were dropped on YPD (1% [w/v] yeast extract, 2% [w/v] bacto peptone, 2% [v/v] glucose (Roth), 3% [w/v] agar (Becton Dickinson)) and YPG media. After incubation at the indicated temperatures the growth plates were photographed and non-relevant growth plate areas were excised digitally indicated by a small gap.

Isolation of mitochondria

Yeast cells were grown in YPG medium at permissive temperature (19-23°C) and shaking with 130 rpm as a preculture. The main yeast culture was inoculated with the preculture and grown under permissive conditions (19-23°C) for 24 hr and shaking at 130 rpm. Yeast cells were harvested in an exponential growth phase at 1,700 x g (4,000 rpm, H-12000, Thermo-Fisher Scientific) for 10 min at room temperature (RT). Cell pellet was resuspended and washed in dH_2O and centrifuged for 5 min at RT and 1,500 x g (3,000 rpm, SLA-3000, Sorvall). Yeast cells were incubated in 2 ml/g wet weight DTT buffer (100 mM Tris(hydroxymethyl)aminomethane (Tris)/H_2SO_4 (MP Biomedicals and Roth), pH 9.4, 10 mM dithiothreitol (DTT, Roth)) for 30 min at 130 rpm and 23°C. Cells were reisolated for 5 min at 2,000 x g (3,500 rpm, SLA-3000, Sorvall) and washed once in sorbitol buffer (16 mM K_2HPO_4 (Roth), 4 mM KH_2PO_4 (Roth), pH 7.4, 1.2 M sorbitol (Roth)). The cell suspension was then treated for 45 min in 6.5 ml/g wet weight sorbitol buffer including 4 mg/ml Zymolyase 20T (Nacalai Tesque, Inc.) at 23°C and 130 rpm. Spheroplasts were isolated and washed once in sorbitol buffer for 5 min at 1,500 x g (3,000 rpm, SLA-3000, Sorvall). The pellet was resuspended in homogenization buffer (0.6 M sorbitol, 10 mM Tris/HCl, pH 7.4, 1 mM ethylenediaminetetraaceticacid (EDTA, Calbiochem), 0.4% [w/v] bovine serum albumin (ChemCruz), 1 mM phenylmethyl sulfonyl fluoride (PMSF, Sigma)) and spheroplasts were mechanically opened on ice by homogenizing 20 times in a glass-Teflon potter. Mitochondria were isolated by differential centrifugation. Cell debris were removed by spinning 2 min 260 x g (1,500 rpm, SA800, Sorvall) followed by 4 min at 1,000 x g (3,000 rpm, SA800, Sorvall) and 4°C. The supernatant was transferred in a fresh tube and spun for 15 min at 1,870 x g (4,000 rpm, SA800, Sorvall). To pellet mitochondria, supernatant was spun for 15 min at 16,800 x g (12,000 rpm, SA800, Sorvall) and 4°C. The mitochondrial pellet was washed in ice cold SEM buffer (250 mM sucrose (MP Biomedicals), 10 mM 3-(*N*-morpholino)propanesulfonic acid (MOPS, Sigma), pH 7.2, 1 mM EDTA) and spun 5 min at 1,870 x g (4,000 rpm, SA800, Sorvall) and 4°C. Supernatant was transferred into a fresh tube and mitochondria were reisolated for 15 min at 16,800 x g (12,000 rpm, SA800, Sorvall) and 4°C. Finally, the mitochondrial pellet was taken up in a small volume of ice cold SEM buffer and the protein concentration was determined by employing the Bradford assay. Mitochondria at 5-10 μg/ml SEM were snap frozen in liquid nitrogen and stored at −80°C.

Site-directed mutagenesis

Single amino acid substitutions in Tim9 and Tim10 were introduced by site-directed mutagenesis. The centromeric plasmid pFL39 containing the open reading frame of *Saccharomyces cerevisiae TIM9* or *TIM10* under the control of their endogenous promoter and terminator (see Key Resources Table) was used as template for a PCR amplification with Q5 polymerase (NEB) and primers encoding the desired mutation (Table S2). After template digest (3 hr, 37°C) with DpnI (NEB), the PCR products were transformed into XL-1 Blue *Escherichia coli* cells (Stratagene). Plasmids of single colonies were isolated by using the QIAprep Spin Miniprep Kit (QIAGENe) and verified by sequencing.

Gel electrophoresis and western blotting

For SDS-PAGE analysis, mitochondria were pelleted (5 min, 20,800 x g, 4°C (14,000 rpm, Eppendorf 5417R)) and resuspended in Laemmli buffer (60 mM Tris, pH 6.8, 2% [w/v] dodecylsulfate-Na-salt (SDS (Serva)), 10% [v/v] glycerol, 0.02% [w/v] bromphenol blue (Sigma)) containing 2 mM PMSF and 2% [v/v] 2-mercaptoethanol and incubated for 5-15 min at 65-95°C at 1,400 rpm. Laemmli samples were either loaded to 15% polyacrylamide gels containing 15% polyacrylamid (Rotiphorese Gel 30 (30% acrylamide, 0.8% bisacrylamide) (Roth)) and run in SDS running buffer (25 mM Tris/HCl, pH 8.8, 191 mM glycine (MP Biomedicals), 1% [w/v] SDS) at 35 mA for 2.5 h or 10% Tris-Tricine polyacrylamide gels containing 10% polyacrylamide (49.5% [w/v] acrylamide (Roth), 3% [w/v] bisacrylamide (Serva)) and run in anode (0.2 M Tris/HCl, pH 8.9) and cathode (0.1 M Tris, 0.1 M tricine (Roth), 0.1% [w/v] SDS, pH 8.25) buffer at 65-80 mA, 600 V for 3-4 h. Afterward, proteins were transferred by standard semi-dry western blot transfer on PVDF membranes (Immobilon-P (Millipore)) at 25 V, 250 mA for 2.5 h in Western transfer buffer (20 mM Tris, 150 mM glycine, 0.02% [w/v] SDS, 20% [v/v] methanol). Prior to antibody decoration, equal loading on the membranes was checked by protein staining (0.2% Coomassie R250 (Roth), 10% [v/v] acetic acid (Roth) and 30% [v/v] ethanol), membranes were destained in 100% methanol, shortly washed in TBST (200 mM Tris/HCl, pH 7.5, 1.25 M $CaCl_2$ (Roth), 0.1% Tween20 (Sigma)) and then incubated for 1 h in 5% [w/v] fat-free dried milk powder (Frema Reform) in TBST at room temperature. Then membranes were incubated for 3 h in the indicated primary antibodies (see Key Resources Table) and 1 h in secondary anti-rabbit IgG antibody (Sigma), diluted 1:10,000 in 5% [w/v] fat-free dried milk powder in TBST. Before and after each antibody decoration, membranes were washed in three 5 min washing steps in TBST. Finally, membranes were incubated in ECL solution (Haan and Behrmann, 2007) and the resulting chemiluminescence signals were detected by a LAS-4000 camera system (Fujifilm).

For blue native PAGE analysis, mitochondria were solubilized for 15 min on ice in digitonin buffer (0.1 mM EDTA, 10% [v/v] glycerol, 50 mM NaCl (Roth), 1 mM PMSF, 20 mM Tris/HCl, pH 7.4, 0.35 - 1% [w/v] digitonin (MATRIX BioScience). Prior loading of the supernatant to a 4-6.5 to 16% discontinuous gradient gel, blue native loading dye (0.5% [w/v] Coomassie blue G (Serva), 50 mM 6-aminocaproic acid (Sigma), 10 mM Bis/Tris (Roth), pH 7) was added. Gel electrophoresis was performed in anode (50 mM Bis/Tris/HCl, pH 7) and cathode buffer (50 mM tricine, pH 7, 15 mM Bis/Tris, 0.02% [w/v] Coomassie G) at 600 V, 15-20 mA/gel for 1.5 - 3.5 h at 4°C. After gel electrophoresis, gels were destained and fixed (50% [v/v] ethanol, 10% [v/v] acetic acid) until protein bands became visible.

Gels were dried and exposed to PhosphorImager screens (GE Healtcare and Fuji) and signals were detected with a FLA7000 scanner (GE Healthcare). Non-relevant gel lanes were excised digitally, as indicated by a small gap. For radioactive SDS samples, gels

were first stained (30% [v/v] ethanol, 10% [v/v] acetic acid, 1% [w/v] Coomassie R250) and destained to compare equal protein loading and then dried and exposed.

In vitro transcription and translation

For *in vitro* translation of ^{35}S-radiolabeled precursor proteins, plasmids carrying a SP6 promoter-binding region followed by the gene of interest were used. Plasmids were incubated with the TNT SP6 quick coupled kit (Promega), an *in vitro* eukaryotic transcription/translation system based on rabbit reticulocytes, and [^{35}S] methionine (PerkinElmer) for 2 hr at 30°C and 300 rpm.

For the *in vitro* translation of [^{35}S]Por1 the Rabbit Reticulocyte Lysate System (Promega) was used. First, mRNA was synthesized by using the mMESSAGE mMACHINE SP6 kit (Invitrogen) and cleaned up by the MEGAclear Transcription Clean-Up kit (Invitrogen). Radiolabeled proteins were translated by using the Rabbit Reticulocyte Lysate System (Promega) for 2 hr at 30°C and 300 rpm.

After translation, 20 mM unlabeled methionine (Roth) and 0.3 M sucrose (MP Biomedicals) were added. Lysate was snap frozen in liquid nitrogen and stored at −80°C.

In vitro import into mitochondria

Radiolabeled precursor proteins were imported into 50 μg mitochondria per reaction (protein amount) in the presence of 100 μl import buffer (3% [w/v] bovine serum albumin (Sigma), 250 mM sucrose, 80 mM KCl (Roth), 5 mM $MgCl_2$, 2 mM KH_2PO_4, 5 mM methionine (Sigma), 10 mM MOPS-KOH (Roth), pH 7.2) with 4 mM ATP (Roche), 4 mM NADH (Roth), 2 mM creatine phosphate (Roche) and 2 mM creatine kinase (Roche). To deplete the membrane potential (-Δψ), AVO mix (8 μM antimycin A (Sigma), 1 μM valinomycin (Sigma), 20 μM oligomycin (Sigma), final concentrations) was added and NADH was excluded (Stojanovski et al., 2007). Finally, 2 to 10% [v/v] of rabbit reticulocyte lysate was added and the import reaction was incubated at 25°C and 300 rpm for indicated time periods. Membrane potential dependent import reactions were stopped with 1 μl AVO mix and transferred on ice. For precursors imported into the mitochondrial matrix or inner membrane, not imported precursor proteins were digested by Proteinase K treatment (22.7 mg/ml; Roche) for 15 min on ice and protease activity was inhibited by addition of 1.78 mM (f.c.) PMSF before mitochondria were reisolated for 5 min at 20,800 x g (14,000 rpm, Eppendorf 5417R) at 4°C. Mitochondria were washed with 100 μl ice cold SEM buffer. Finally, mitochondria were either resuspended in Laemmli buffer (0.2 M Tris, pH 6.8, 2% [w/v] SDS, 4% [v/v] glycerol, 12.5% [w/v] bromphenol blue, 1 mM PMSF) or solubilized in digitonin buffer (20 mM Tris/HCl, pH 7.4, 0.1 mM EDTA, 50 mM NaCl, 10% [v/v] glycerol, 0.35%–1.75% digitonin), to be analyzed either on SDS-PAGE or blue native PAGE.

For analysis of carrier precursor binding by TIM9·10 complex by a precursor arrest at the translocase of the outer mitochondrial membrane (TOM), the radiolabeled carboxyl-terminal fusion protein of Aac2 and DHFR (dihydrofolate reductase) was imported according to Ryan et al. (1999).

Membrane potential assessment

The membrane potential (Δψ) of isolated mitochondria was assessed by fluorescence quenching using the luminescence spectrometer Aminco Bowman II (Thermo Electron Corporation). Mitochondria were incubated in 3 mL potential buffer (0.6 M Sorbitol, 0.1% [w/v] BSA, 10 mM $MgCl_2$, 0.5 mM EDTA, 16 mM K_2HPO_4, 4 mM KH_2PO_4, pH 7.4) in the presence of 5 mM L-malate (Sigma), 5 mM succinate (Sigma) and 3 μl DiSC3 (3,3′-dipropylthiadicarbocyanine iodide (Invitrogen)). Absorption was measured by an excitation of 622 nm and an emission of 670 nm until the distribution equilibrium was reached and 3 μl 1 mM valinomycin were added to dissipate the membrane potential.

QUANTIFICATION AND STATISTICAL ANALYSIS

General considerations about quantitative analysis of NMR data

Quantitative NMR data, such as HETSOFAST data, CPMG relaxation dispersion or relaxation data have been based on analyses of peak integrals, determined in CCPNMR (Vranken et al., 2005), and subsequent analyses in in-house written python scripts, unless stated otherwise. Generally, error margins on peak integrals have been determined from the spectral noise (generally 3 times the standard deviation of spectral noise was used), and Monte Carlo analysis of the fit data.

Diffusion ordered NMR spectroscopy

Diffusion coefficients were obtained from a series of methyl-detected DOSY NMR experiments. The integrated intensity as a function of the gradient strength was used to fit the diffusion coefficient (D) using the following equation:

$$I = I_0 \cdot \exp\left(- D \cdot \gamma_H^2 \cdot g^2 \cdot \delta^2 \cdot (D - \delta/3 - \tau/2)\right),$$

where I is the peak integral, γ_H is the gyromagnetic ratio of protons, g is the gradient strength in Gauss/cm, and Δ, δ and τ are delays in the pulse sequence as described in Didenko et al. (2011).

Methyl order parameter measurements from relaxation-violated coherence transfer NMR

Order parameters of methyl axes were obtained from triple-quantum relaxation experiments. The ratio of peak integrals in the relaxation-violated coherence transfer (I_a) and the reference experiment (I_b) as a function of the relaxation delay T were fitted according to Equation 7 of Sun et al. (2011):

$$I_a/I_b = \frac{3}{4}\frac{\eta \tanh\left(\sqrt{\eta^2+\delta^2}\,T\right)}{\sqrt{\eta^2+\delta^2}-\delta \tanh\left(\sqrt{\eta^2+\delta^2}\,T\right)}$$

A grid-search procedure was implemented in an in-house written python program to extract η and δ, where δ is an empirical fit constant. The product of methyl-axis order parameter and overall correlation time constant, $S^2_{axis}\tau_c$, can be calculated from η using the following relationship, which contains only known physical constants, according to Equation 1 of Sun et al. (2011):

$$\eta \approx 0.9\left(\frac{\mu_0}{4\pi}\right)[P_2(\cos\Theta_{axis,HH})]^2\frac{S^2_{axis}\gamma_H^4\hbar^2\tau_c}{r^6_{HH}}$$

The physical constants are $\gamma_H = 2.67522.10^8\ s^{-1}.T^{-1}$, $r_{HH} = 1.813$ Å, $\theta_{axis,HH} = 90$ degrees, $\mu_0 = 4\pi.10^{-7}\ H.m^{-1}$ and P_2 denotes the second-order Legendre polynomial.

Error margins of the fitted parameters were obtained using a standard Monte Carlo procedure. Hereby, 1000 synthetic datasets were generated, by adding random noise (within the experimentally determined noise levels) onto the data points that were back predicted from the best-fit parameters. These 1000 datasets were fitted analogously to the experimental data, to extract the standard deviation over these fitted parameters. The raw data and analysis scripts have been deposited in the Mendeley data repository (see Key Resources Table).

CPMG experiments

CPMG profiles, R_{2eff} as a function of ν_{CPMG}, were fitted with a numerical approach, using the program ChemEx (version 0.6.0, available at https://github.com/gbouvignies/chemex/releases), in order to obtain a global exchange rate constant, k_{ex}, and site-specific chemical-shift differences $|\Delta\omega|$. The two-state exchange model was used as an approximation, and the populations of the two exchanging states were set to 50%. The CPMG RD profiles of ALV TIM in its apo state and bound to Ggc1 and Aac3 have been deposited in the Mendeley data repository.

In vitro import experiments

For quantification of *in vitro* imports experiments ^{35}S-labeled proteins or complexes were quantified by autoradiography with Multi Gauge (Fujifilm, Version 3.2). Experiments were performed in triplicate (n = 3) and the error bars indicate the standard error of the mean (SEM). Overlapping error bars were slightly shifted on the x axis for enhanced visibility.

DATA AND SOFTWARE AVAILABILITY

NMR resonance assignments have been deposited in the BioMagResBank. The accession number for the resonance assignment is BioMagResBank: 27052. The accession number for SAXS data are SASBDB: SASDEF2 (TIM910) and SASBDB: SASDEG2 (TIM910/Ggc1). CPMG relaxation dispersion data have been deposited in Mendeley data. Accession numbers can be found in the Key Resources Table.

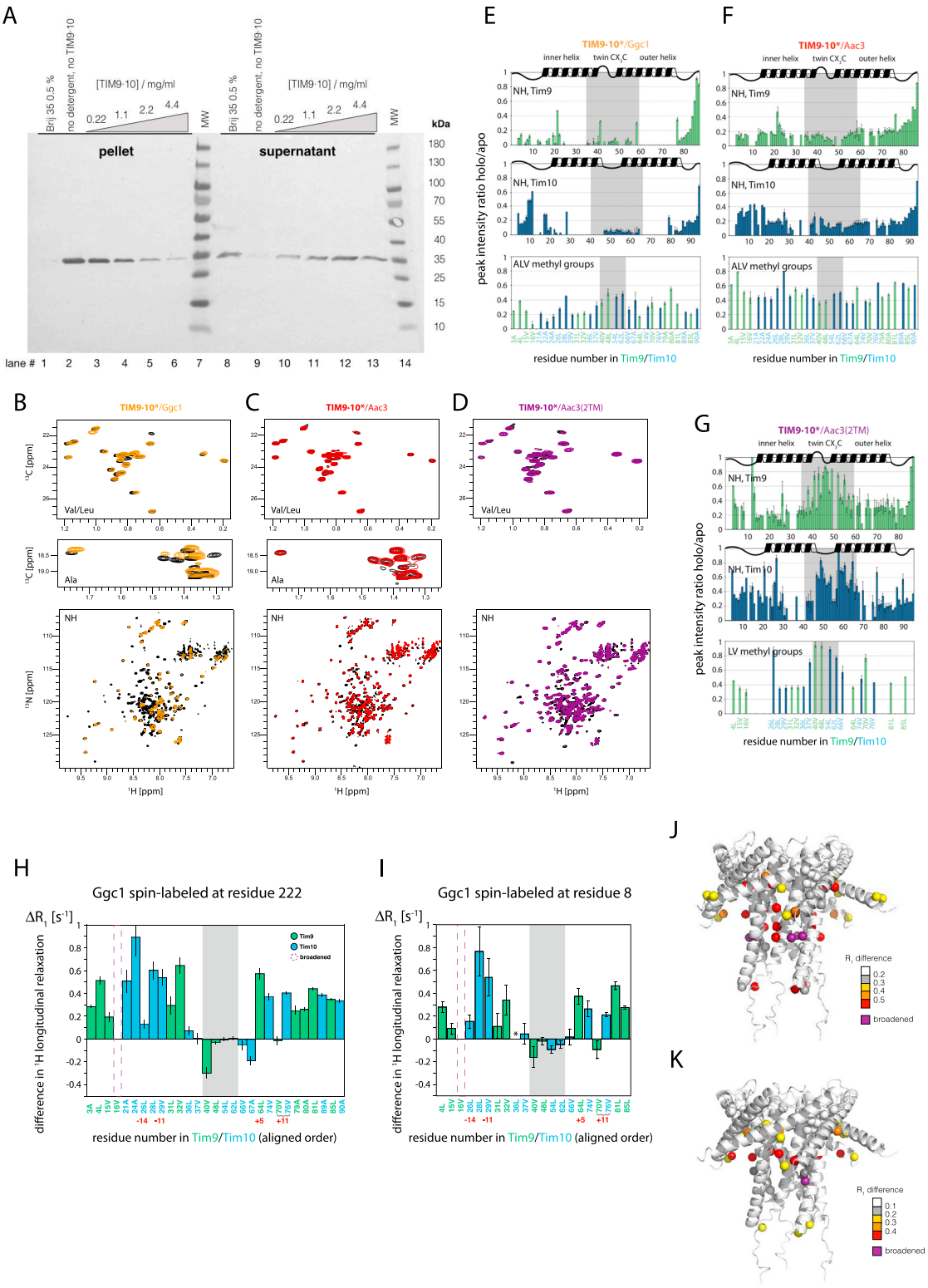

Figure S1. Formation and Characterization of TIM9·10 Binding Mitochondrial Carriers, Related to Figure 1

(A) Production of TIM9·10/Ggc1 using a cell-free protein production reaction mixture containing the expression plasmid encoding the Ggc1 sequence, complemented by either detergent (Brij35) or different concentrations of TIM9·10. The latter was expressed in *E. coli* and purified using standard procedures described in the Methods section. The amount of His-tagged Ggc1 in solution or in the insoluble pellet was analyzed by SDS-PAGE and immunodecoration with

(legend continued on next page)

anti-His antibody. In the presence of detergent (without TIM9·10), Ggc1 is found exclusively in the soluble fraction (lane 8). In the absence of detergent and chaperone (lanes 2 and 9), Ggc1 is found only in the pellet, as expected for a highly aggregation-prone polypeptide. With increasing amounts of TIM9·10 (lanes 10-13) the amount of Ggc1 in solution increases, while the amount in the pellet decreases (lanes 3-6). This data shows that recombinantly expressed TIM9·10 is functional and allows retaining Ggc1 in solution in a concentration-dependent manner.

(B-D) Relative peak intensities of NMR signals of TIM9·10 in complex with Ggc1 (orange), Aac3 (red) or Aac3(2TM) (purple).

(E-G) Backbone HN and ALV methyl spectra of TIM9·10 in apo and holo complexes, corresponding to the data shown in B – D. Precursor protein binding leads only to small changes of peak positions, but leads to strong reduction of the peak intensities. Note that numerous backbone NH sites are broadened beyond detection, in particular in the hydrophobic cleft. The higher peak intensities in the TIM9·10/Aac3(2TM) sample, compared to full-length Aac3 and Ggc1, is ascribed to the fact that Aac3(2TM) recruits only one TIM9·10 hexamer, thus resulting in a smaller complex.

(H and I) Paramagnetic relaxation enhancement (PRE, proton-ΔR_1) effects at ALV methyl sites on TIM9·10 induced by two different paramagnetically-tagged Ggc1 precursor proteins bound to TIM9·10, where the MTSL spin label is attached to either C222 or C8 of Ggc1. ΔR_1 is obtained as the difference of R_1 measured with bound MTSL-labeled Ggc1, and the corresponding relaxation rate constant in the same sample after reduction of the spin label by addition of ascorbic acid. The resonance of Val16 is broadened beyond detection (indicated in purple). In the dataset shown in (I), residue L36 is not graphically shown due to its large error margin; its value is 0.097 ± 0.5. All error margins shown in this figure were determined from 3 times the spectral noise level.

(J and K) The observed PRE effects are plotted onto the structure of TIM9·10 in (MTSL at C222 in J) and (MTSL label at C8 in K).

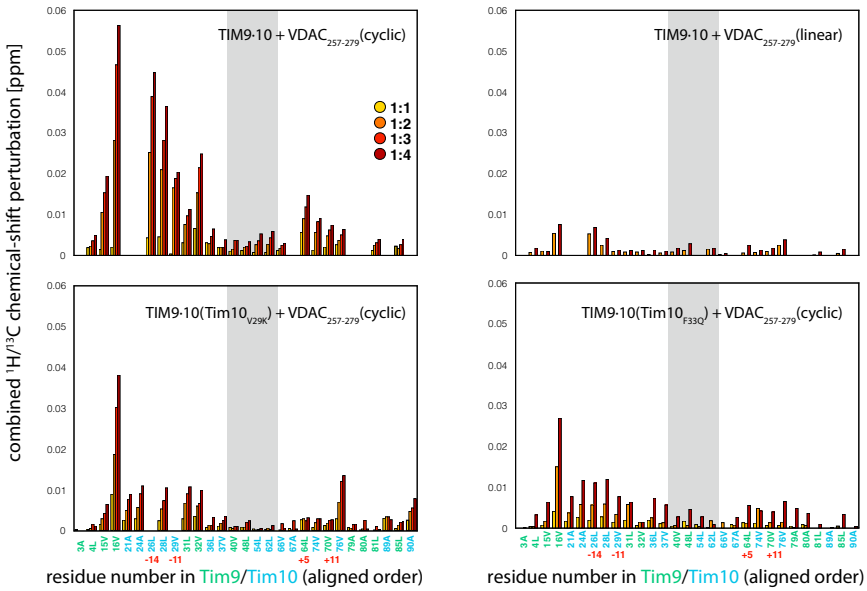

Figure S2. Binding of VDAC$_{257-279}$ Peptides to Wild-Type and Mutant TIM9·10, Related to Figure 2

The protein constructs, (WT, or mutations V29K or F33Q of the Tim10 subunits) are indicated, as well as the identity of the peptide (linear, cyclic). Titration points with different concentrations of VDAC$_{257-279}$ peptides (at a constant TIM9·10 concentration of 200 μM) are shown with different colors.

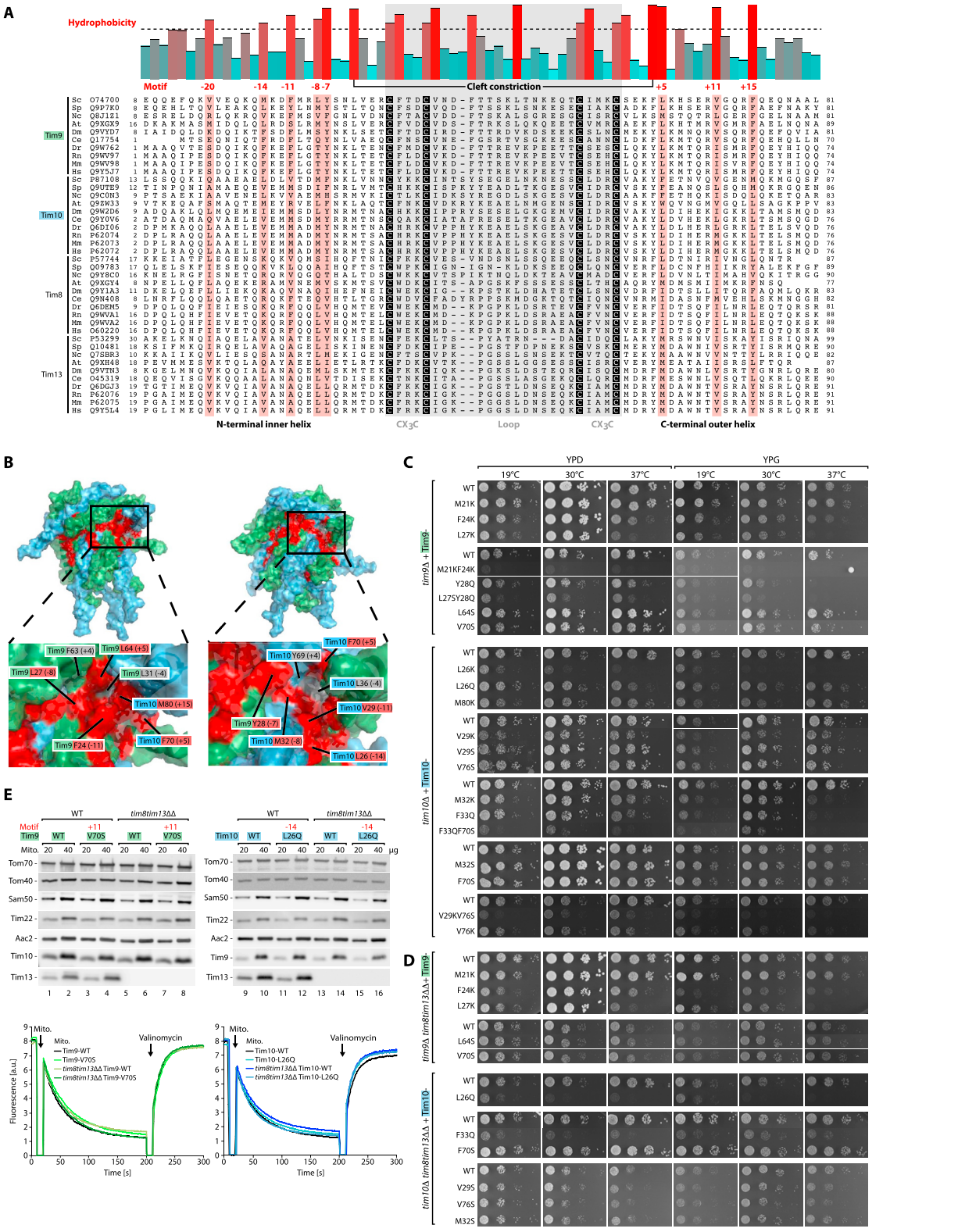

(legend on next page)

Figure S3. Characterization of Yeast Cells Expressing *tim9* and *tim10* Variants of the Conserved Motif, Related to Figures 3A, 3C–3F, 4A–4E, and 5A–5D

(A) Conserved motif (red) of soluble intermembrane space TIM chaperones in the inner N-terminal and outer C-terminal helices. The bar graph indicates the mean hydrophobicity (software Geneious, Biomatters) of the aligned sequences. Sc, *Saccharomyces cerevisiae*; Sp, *Schizosaccharomyces pombe*; Nc, *Neurospora crassa*; At, *Arabidopsis thaliana*; Dm, *Drosophila melanogaster*; Ce, *Caenorhabditis elegans*; Dr, *Danio rerio*; Rn, *Rattus norvegicus*; Mm, *Mus musculus*; Hs, *Homo sapiens*.

(B) Magnification of the TIM9·10 cleft constriction interaction face showing in gray the buried residues at position −4 (Tim9 L31 and Tim10 L36) and +4 (Tim9 F63 and Tim10 Y69) and in red the conserved hydrophobic residues of the binding motif.

(C) Original data of *tim9* and *tim10* mutant growth phenotypes. Growth was analyzed either on glucose (YPD) or glycerol (YPG) containing agar media at 19°C, 30°C or 37°C. This supplementary figure shows the original data for Figure 3C and contains data from Figure 3F for comparison.

(D) Original data of *tim9* and *tim10* mutant growth phenotypes in *tim8tim13*ΔΔ background related to Figure 3E analyzed as described in C.

(E) Steady state protein amounts and membrane potential of isolated TIM chaperone mutant mitochondria are comparable to WT. Upper panels: Mitochondria isolated from yeast cells grown at permissive temperature, were analyzed by SDS-PAGE and immunodecoration against indicated antibodies. Lower panels: Membrane potential was assessed by fluorescence quenching and dissipated by the addition of valinomycin.

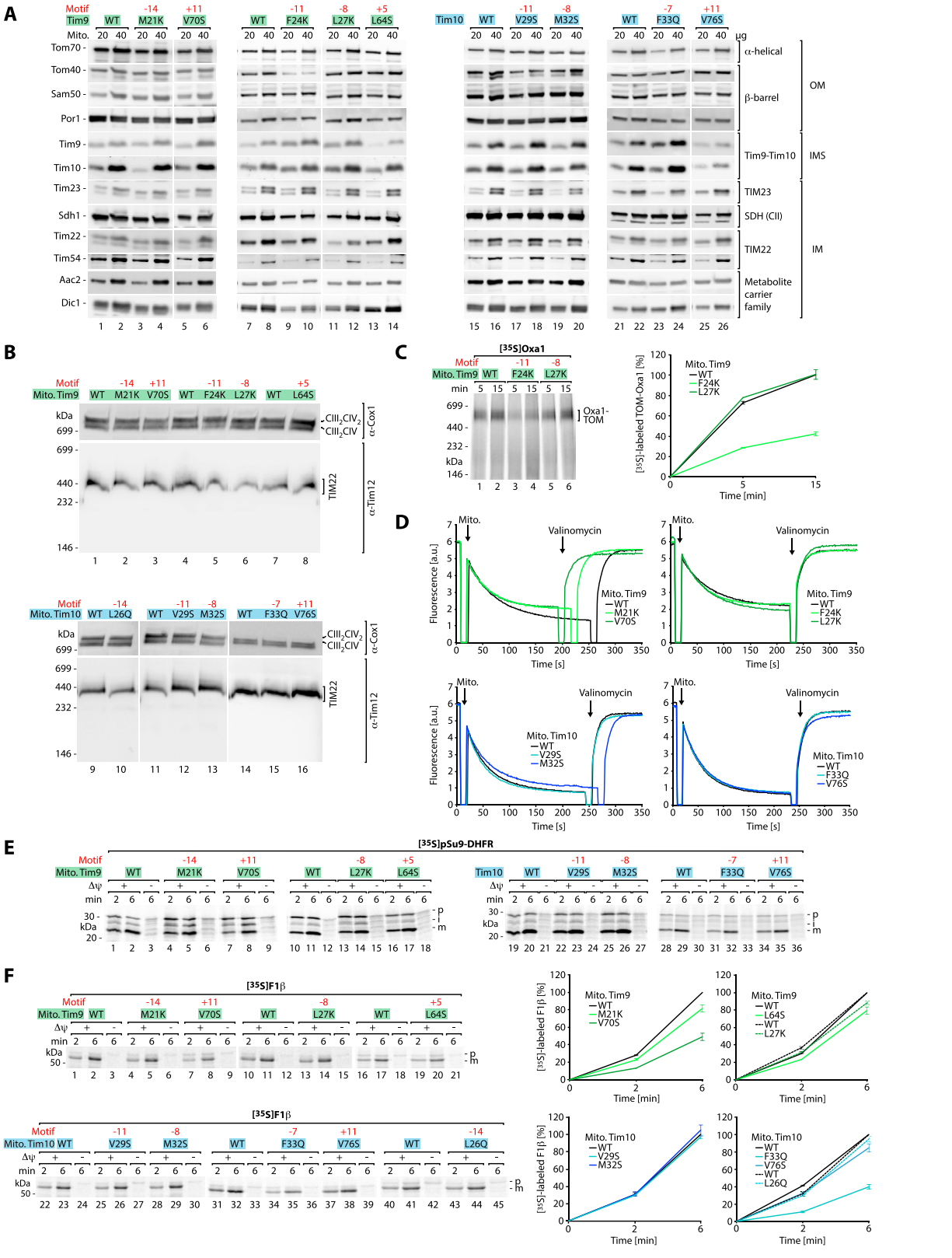

(legend on next page)

Figure S4. Analysis of Mitochondria Expressing *tim9* and *tim10* Variants of the Conserved Motif, Related to Figures 3E, 4A–4E, and 5A–5D

(A) Steady state protein amounts of isolated TIM chaperone mutant mitochondria in *tim8tim13*ΔΔ background. Mitochondria were analyzed as described for Figure S3E. OM, outer mitochondrial membrane; IMS, intermembrane space; IM, inner mitochondrial membrane; SDH (CII), succinate dehydrogenase (complex II of the respiratory chain); TIM23, presequence translocase of the inner membrane; TIM22, carrier translocase of the inner membrane.

(B) Steady state protein complexes of isolated TIM chaperone mutant mitochondria in *tim8tim13*ΔΔ background. Mitochondria isolated from yeast cells grown at permissive temperature, were analyzed by BN-PAGE and immunodecoration against indicated antibodies. $CIII_2$-CIV and $CIII_2$-CIV_2, respiratory chain supercomplexes.

(C) [^{35}S]Oxa1 was imported into isolated mitochondria of *tim9* mutants in *tim8tim13*ΔΔ background after dissipation of the membrane potential and analyzed by blue native PAGE. The [^{35}S]Oxa1-TOM intermediate was quantified by autoradiography (SEM, n = 3 experiments).

(D) Mitochondrial membrane potential of TIM chaperone mutant mitochondria is comparable to WT. Membrane potential was assessed as in Figure S3E.

(E) Matrix protein import into TIM chaperone motif mutant mitochondria in *tim8tim13*ΔΔ background. The import of the presequence-carrying matrix protein [^{35}S] pSu9-DHFR into mitochondria was analyzed on SDS-PAGE followed by autoradiography. p, precursor; i, intermediate; m, mature; $\Delta\psi$, mitochondrial membrane potential.

(F) Analysis of [^{35}S]$F_1\beta$(ATP2) import as described for E. The mature band was quantified by autoradiography (SEM, n = 3 experiments).

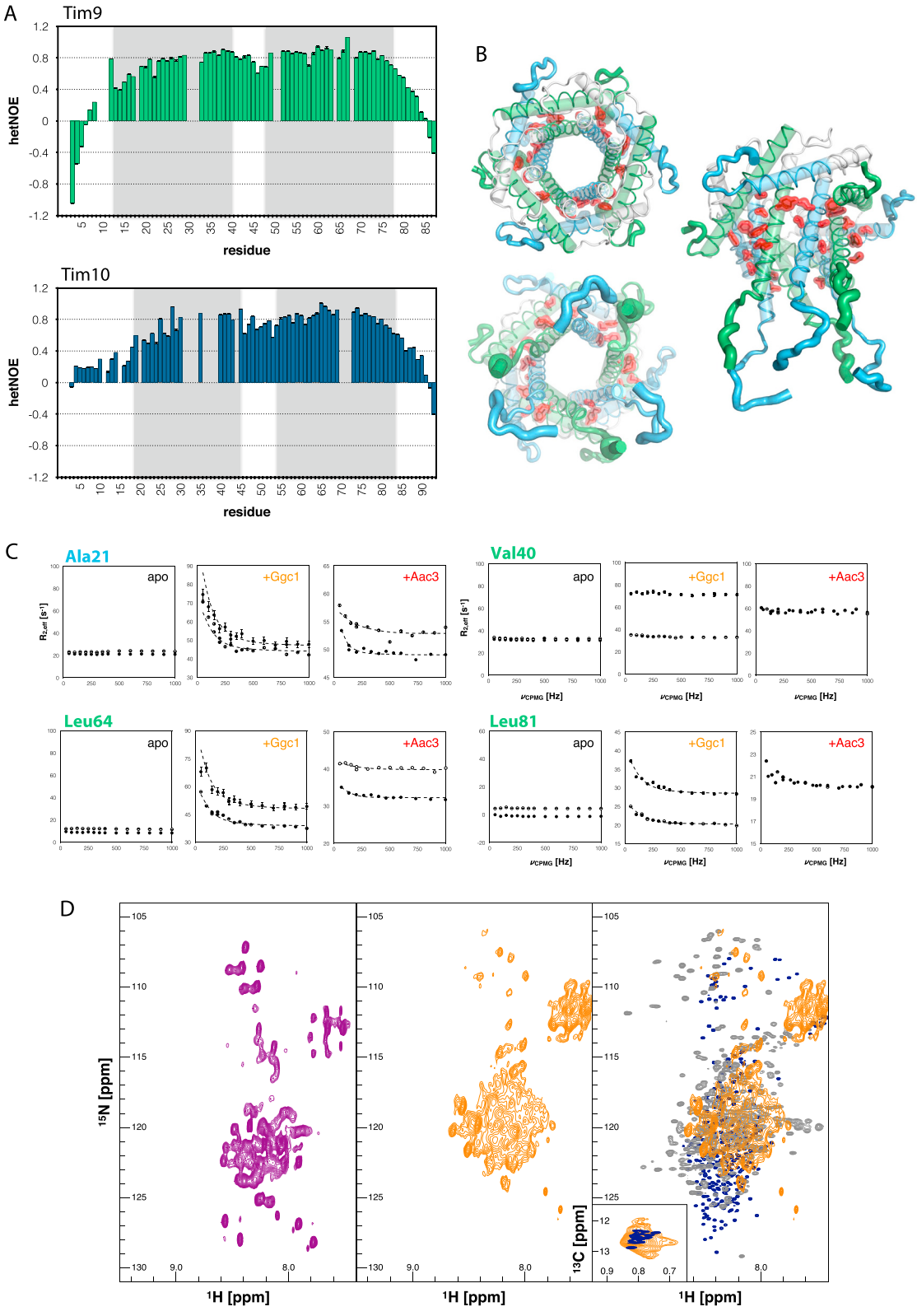

(legend on next page)

Figure S5. Dynamics of apo TIM9·10 and Precursor Protein Bound to TIM9·10, Related to Figures 6C and 6G

(A) ^{1}H-^{15}N heteronuclear NOE effect in apo TIM9·10, shown for all available backbone amide sites in Tim9 (top) and Tim10 (bottom).

(B) Graphical representation of the motional amplitudes sampled in an unbiased one-microsecond-long all-atom MD simulation of TIM9·10 using the Amber ff99SB*-ILDN force field. The width of the backbone representation reflects the root mean square fluctuation (RMSF) at residue level averaged over the RMSF values of Tim9 and Tim10 monomers by considering the symmetry.

(C) Representative CPMG relaxation dispersion curves of four residues in TIM9·10 in apo and holo states.

(D) ^{1}H-^{15}N NMR spectra of deuterated carrier precursor proteins bound to unlabeled TIM9·10. Left: ^{1}H-^{15}N BEST-TROSY (Favier and Brutscher, 2011) spectrum of Aac3(2TM) bound to TIM9·10. Middle: ^{1}H-^{15}N CRINEPT-TROSY (Riek et al., 1999) of Ggc1 bound to TIM9·10 recorded in an overnight experiment at 35°C. The sensitivity of an INEPT-based TROSY experiment was significantly lower without providing additional cross-peaks (data not shown). Right: Overlay of ^{1}H-^{15}N correlation spectra of Ggc1 solubilized in 8 M urea (blue), where it is unfolded, approx. 50 mM dodecylphosphocholine (DPC), where it forms primarily helical structure (gray) (Kurauskas et al., 2018) and bound to TIM9·10 (orange). Insert in right spectrum: ^{1}H-^{13}C HMQC spectrum of the Ile-δ1 sites in Ggc1 (labeled at methyls of Ile-δ1 and Ala-β). The Ala part of this spectrum is displayed in Figure 6G. In the urea-unfolded state, Ggc1 shows very sharp resolved peaks and a narrow ^{1}H peak dispersion, both typical for a fully flexible random-coil state. The broader dispersion in the DPC-refolded state, points to a more compact arrangement with at least some tertiary contacts. The comparison to these states allows us to exclude that Ggc1 bound to TIM is a fully flexible 'random coil' state, and it indicates a substantial degree of conformational heterogeneity. Note that across the accessible range of temperatures (ca. 5 to 50°C), the spectra quality does not significantly change, indicating the presence of μs-ms exchange over these temperatures, and excluding more advanced NMR experiments for site-specific analyses of secondary structure.

All error margins shown in (A) and (C) were determined from 3 times the spectral noise level.

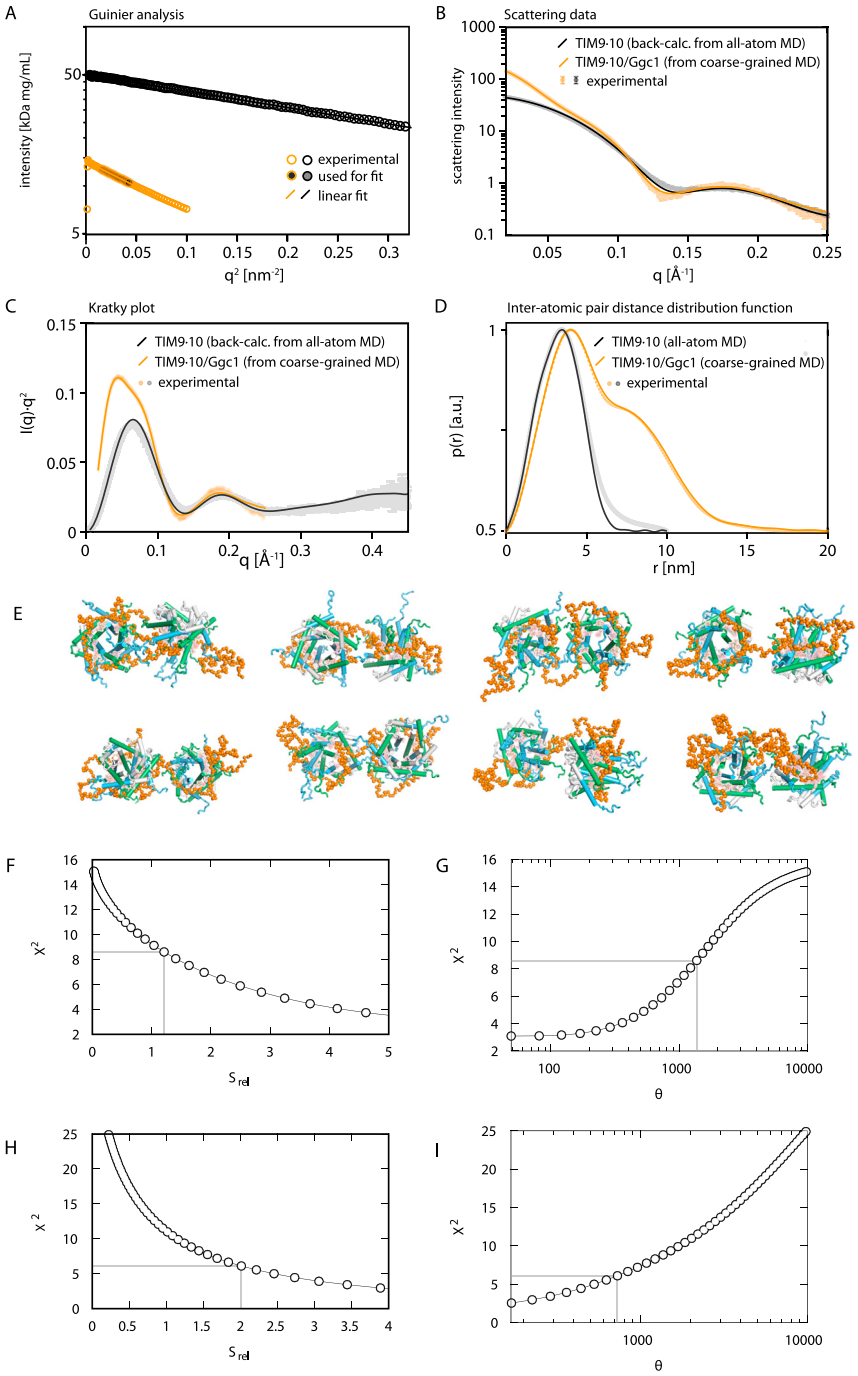

Figure S6. SAXS Data of TIM9·10 and TIM9·10/Ggc1 Complexes and Molecular Dynamics Analysis, Related to Figures 7C and 7E

(A) Guinier analysis of the SAXS data of apo TIM9·10 (black) and TIM9·10/Ggc1 (orange).

(B) The experimental scattering curves of apo TIM9·10 (black) and TIM9·10/Ggc1 complexes (orange) are compared with the scattering curves back-calculated from the reweighted all-atom MD ensemble of apo TIM9·10 and coarse-grained MD ensemble of the TIM9·10/Ggc1 complex, respectively. The χ^2 values between experimental curves and calculated curves of reweighted MD ensemble are 8.6 and 6.1 for the apo and holo TIM complexes, respectively.

(C and D) show the Kratky plots and the pair-distance distributions transformed from the scattering data. Note that the deviation for the apo TIM9·10 hexamer might be caused by the imperfection of the current force field.

(legend continued on next page)

(E) Eight different initial models of the TIM9·10/Ggc1 complex used for coarse-grained MD simulations.
(F-I) SAXS guided MD ensemble refinement of the apo TIM9·10 hexamer F, G and the TIM9·10/Ggc1 complex H, I using the maximum entropy approach. F and H show $\chi 2$ as a function of the relative entropy Srel. G and I show $\chi 2$ as a function of the 'temperature-like' free parameter θ. The gray lines indicate the resulted $\chi 2$ and Srel with a proper choice of θ.